Posted on 16 Dec 2022 — The copyright holder is the author/funder. All rights reserved. No reuse without permission. — https://doi.org/10.22541/essoar.167117623.37432358/v1 — This a preprint and has not been peer reviewed. Data may be preliminary.

A novel efficient method of estimating suspended total sediment load fraction in natural rivers

Hyoseob Noh[1], Yong Sung Park[1], and Il Won Seo[1]

[1]Seoul National University

December 16, 2022

Abstract

Sediment transport load monitoring is important in civil and environmental engineering fields. Monitoring the total load is difficult, especially because of the cost of the bed load transport measurement. This study proposes estimation models for the suspended load to total load ratio (Fsus) using dimensionless hydro-morphological variables. Two prominent variable combinations were identified using the recursive feature elimination procedure of support vector regression (SVR): (1) W/h, d*, Reh, Frd, and Rew and (2) Reh, Fr, and Frd. The explicit interactions between Fsus and the two combinations were revealed by two modern symbolic regression methods: multi-gene genetic programming and Operon. The five-variable SVR model showed the best performance (R2=0.7722). The target dataset was clustered by applying a self-organizing map and Gaussian mixture model. Through these steps, Reh and Frd are determined as the two most influential variables. Subsequently, the one-at-a-time sensitivity of the input variables of the empirical models was investigated. By referring to the clustering and sensitivity analyses, this study provides physical insights into Fsus controlling relationships. For example, Fsus is proportional to Reh and is inversely related to Frd. The empirical models developed in this study are applicable in practice and easy to implement in other real-time surrogate suspended-sediment monitoring methods, because they only require basic measurable hydro-morphological variables, such as velocity, depth, width, and mean bed material grain size.

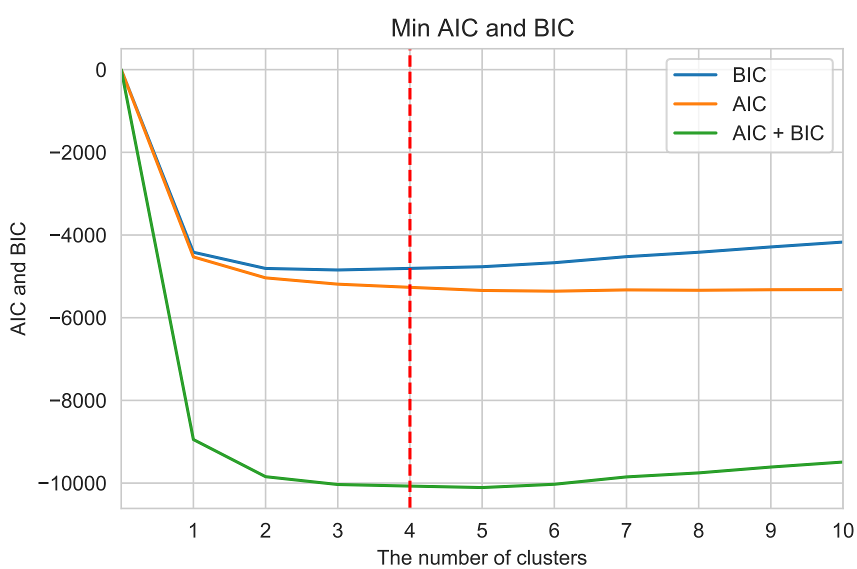

Posted on 16 Dec 2022 — The copyright holder is the author/funder. All rights reserved. No reuse without permission. — https://doi.org/10.22541/essoar.167117623.37432358/v1 — This a preprint and has not been peer reviewed. Data may be preliminary.

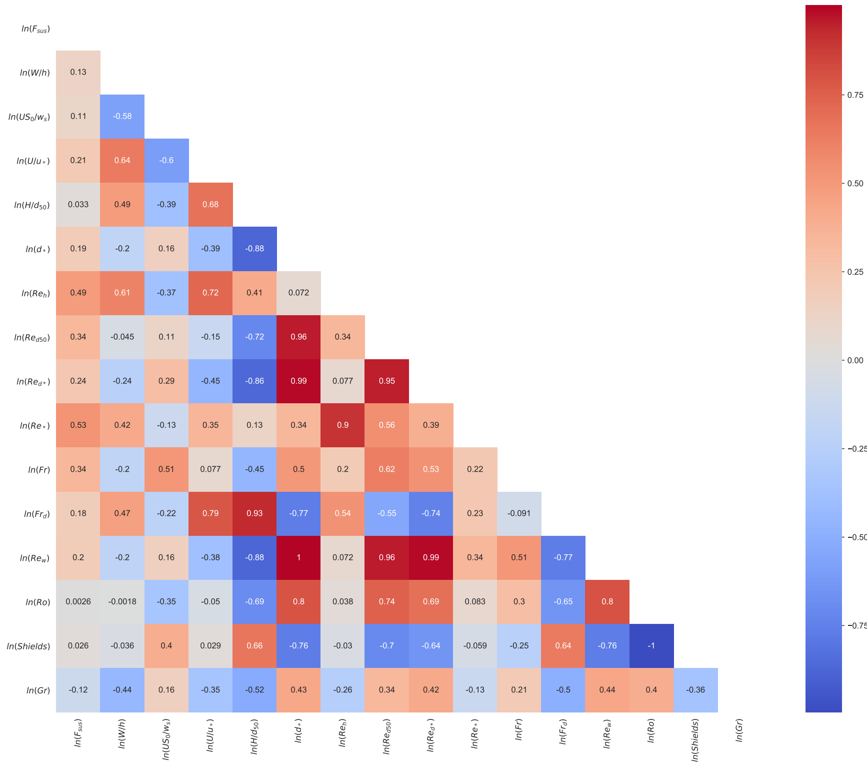

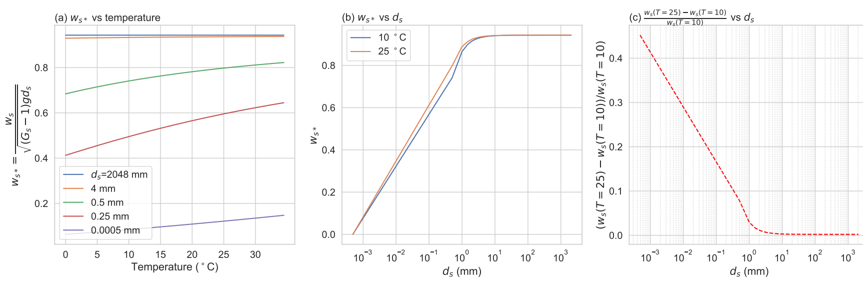

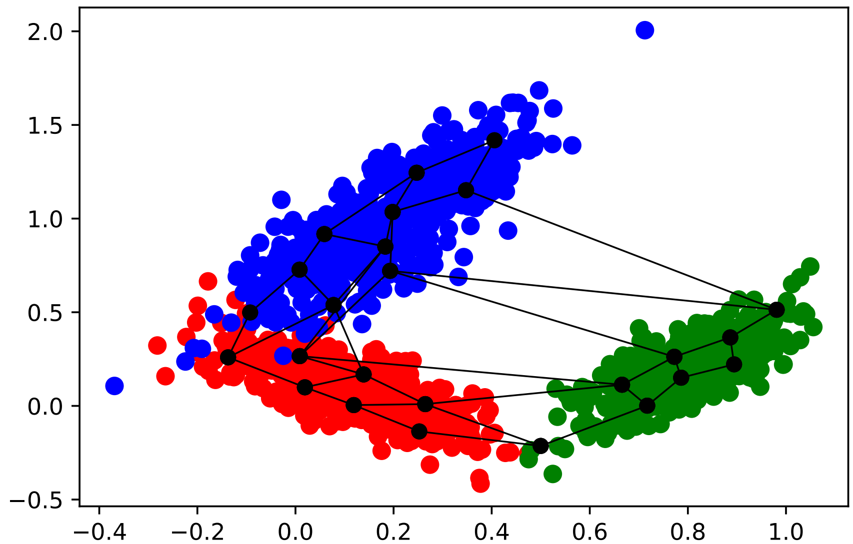

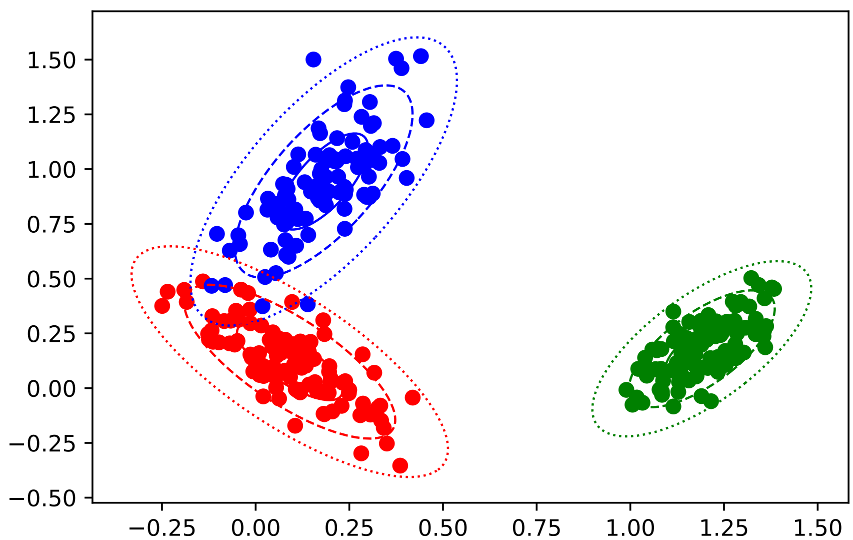

Posted on 16 Dec 2022 — The copyright holder is the author/funder. All rights reserved. No reuse without permission. — https://doi.org/10.22541/essoar.167117623.37432358/v1 — This a preprint and has not been peer reviewed. Data may be preliminary.

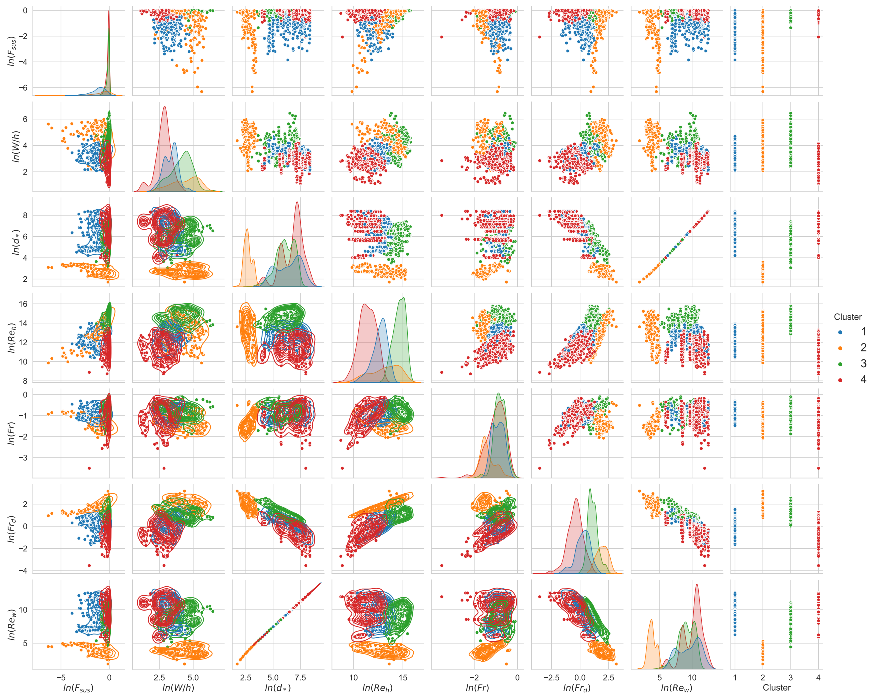

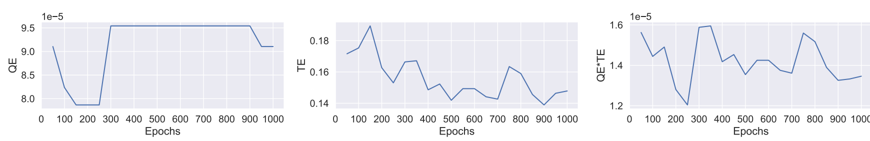

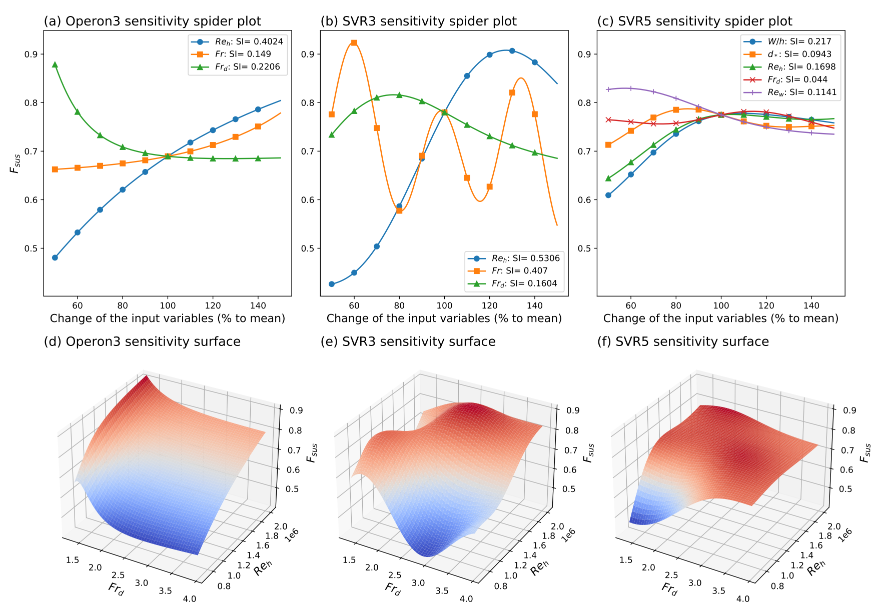

Posted on 16 Dec 2022 — The copyright holder is the author/funder. All rights reserved. No reuse without permission. — https://doi.org/10.22541/essoar.167117623.37432358/v1 — This a preprint and has not been peer reviewed. Data may be preliminary.

Posted on 16 Dec 2022 — The copyright holder is the author/funder. All rights reserved. No reuse without permission. — https://doi.org/10.22541/essoar.167117623.37432358/v1 — This a preprint and has not been peer reviewed. Data may be preliminary.

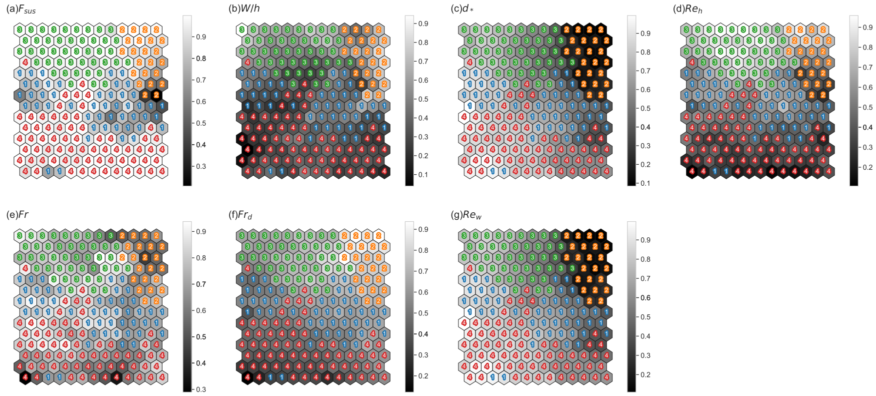

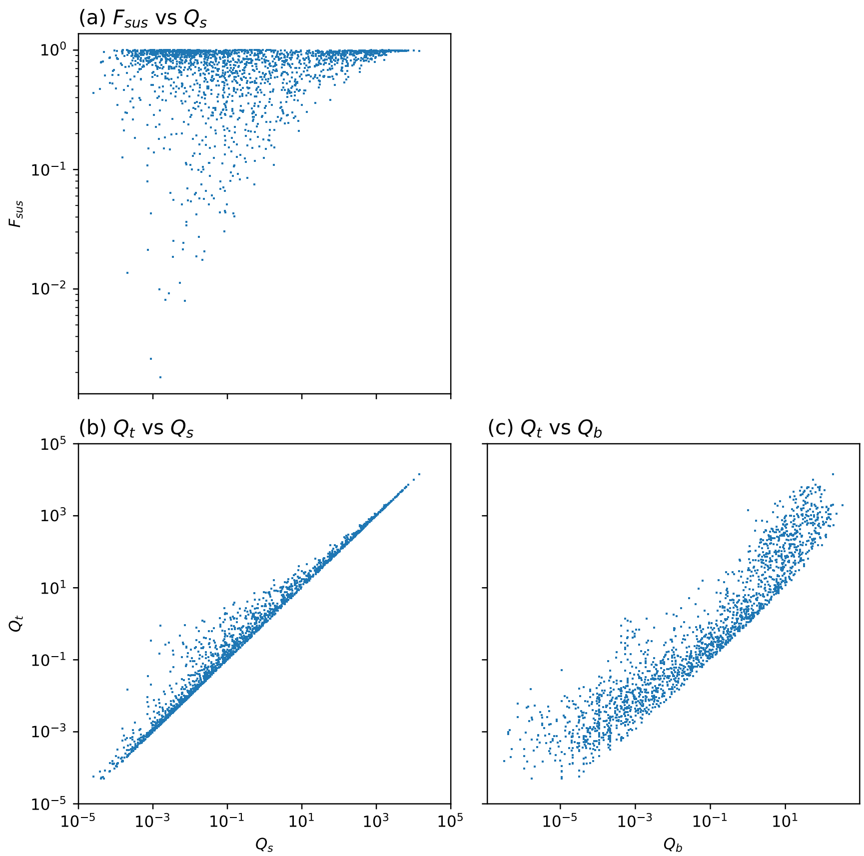

Posted on 16 Dec 2022 — The copyright holder is the author/funder. All rights reserved. No reuse without permission. — https://doi.org/10.22541/essoar.167117623.37432358/v1 — This a preprint and has not been peer reviewed. Data may be preliminary.

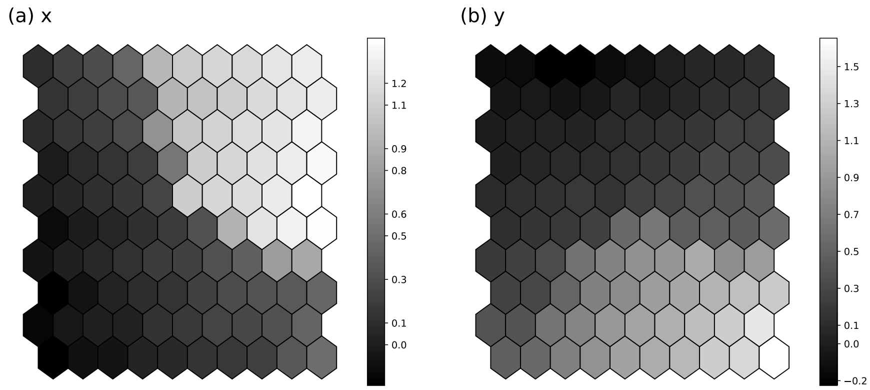

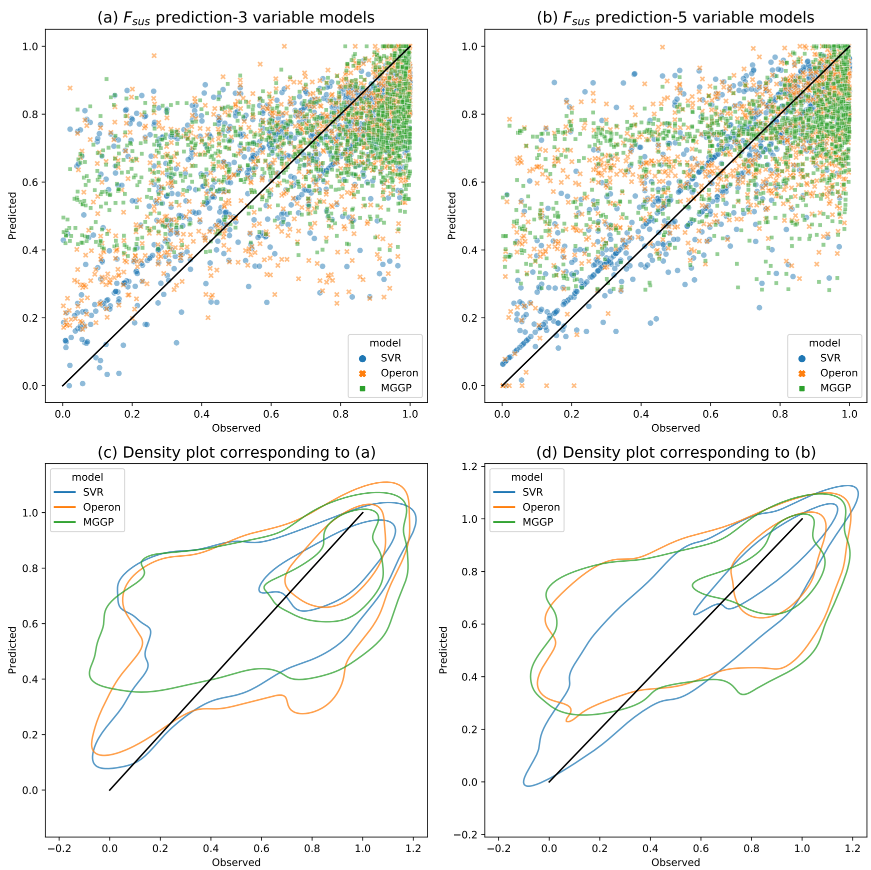

Posted on 16 Dec 2022 — The copyright holder is the author/funder. All rights reserved. No reuse without permission. — https://doi.org/10.22541/essoar.167117623.37432358/v1 — This a preprint and has not been peer reviewed. Data may be preliminary.

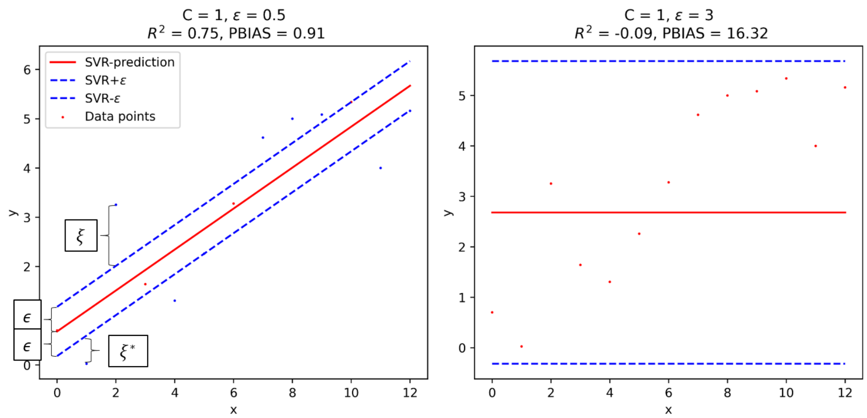

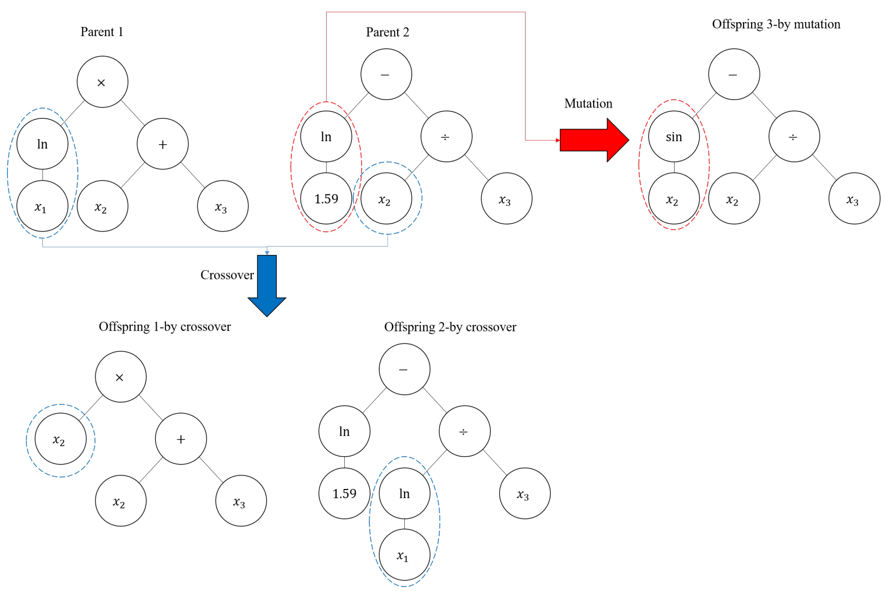

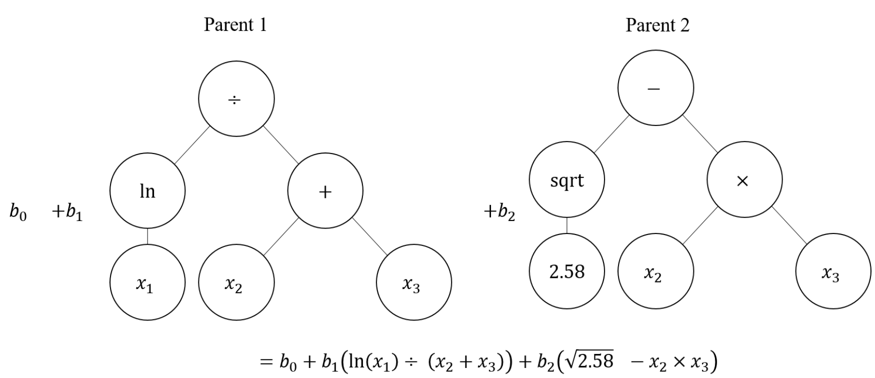

A novel efficient method of estimating suspended total sediment load fraction in natural rivers

Hyoseob Noh[1], Yong Sung Park[1,2], and Il Won Seo[2]

[1]Department of Civil and Environmental Engineering, Seoul National University, Seoul, South Korea
[2]Institute of Construction and Environmental Engineering, Seoul National University, Seoul, South Korea

Key Points:

- Empirical models were developed to estimate the ratio of suspended sediment load to total load using three different machine-learning models
- This study provides physical interpretations of the explicit equations of MGGP and Operon and conducts clustering and sensitivity analyses
- The flow Reynolds and densimetric Froude numbers are the two dominant parameters and SVR5 and Operon3 are practically suitable models

Corresponding author: Yong Sung Park, `dryspark@snu.ac.kr`

Abstract

[Sediment transport load monitoring is important in civil and environmental engineering fields. Monitoring the total load is difficult, especially because of the cost of the bed load transport measurement. This study proposes estimation models for the suspended load to total load ratio (F_{sus}) using dimensionless hydro-morphological variables. Two prominent variable combinations were identified using the recursive feature elimination procedure of support vector regression (SVR): (1) W/h, d_*, Re_h, Fr_d, and Re_w and (2) Re_h, Fr, and Fr_d. The explicit interactions between F_{sus} and the two combinations were revealed by two modern symbolic regression methods: multi-gene genetic programming and Operon. The five-variable SVR model showed the best performance ($R^2 = 0.7722$). The target dataset was clustered by applying a self-organizing map and Gaussian mixture model. Through these steps, Re_h and Fr_d are determined as the two most influential variables. Subsequently, the one-at-a-time sensitivity of the input variables of the empirical models was investigated. By referring to the clustering and sensitivity analyses, this study provides physical insights into F_{sus} controlling relationships. For example, F_{sus} is proportional to Re_h and is inversely related to Fr_d. The empirical models developed in this study are applicable in practice and easy to implement in other real-time surrogate suspended-sediment monitoring methods, because they only require basic measurable hydro-morphological variables, such as velocity, depth, width, and mean bed material grain size.]

1 Introduction

The interactions between sediment transport, flow, and geological characteristics are strongly correlated with channel variation. The alluvial total sediment loads are not only crucial to river systems but are also the main source of coastal sediment (Ouillon, 2018). Therefore, understanding and monitoring sediment transport are of substantial interest to civil and environmental engineers. However, it is challenging to monitor the total load.

The total sediment load Q_t is regarded as the sum of the suspended Q_s and bed Q_b loads. The conventional sediment monitoring process consists of field sampling and sample analysis in a laboratory, which is labor-intensive. In particular, monitoring bed loads is costlier than monitoring suspending loads. Alternative methods to monitor suspended sediment have been proposed that utilize various equipment, such as optical sensors (Agrawal & Pottsmith, 2000) and hyperspectral cameras (Kwon, Seo, et al., 2022, 2022), enabling high spatiotemporal resolution monitoring in the simplified monitoring process. Technological advances in the monitoring of bed loads are comparatively slower than those achieved for suspended loads, owing to the analogous complexity of bed loads. Specifically, suspended loads can be easily calibrated with optical features using turbidity or reflectances, which are readily measured remotely.

For these reasons, the total loads are estimated using the large weights of the suspended loads (Turowski et al., 2010). One popular approach is the modified Einstein procedure (MEP) (Colby & Hembree, 1954), which estimates the total load using suspended sediment transport information and its computer program implementation called the Bureau of Reclamation Automated MEP (Holmquist-johnson, 2006) is available. However, MEP has problems, such as arbitrarily defined terms, physically impossible results ($Q_s > Q_t$), and Rouse number (Ro) tuning. Thus, because of some improbable results and estimation difficulty in using MEP, it has been revised to the series expansion MEP (SE-MEP) for depth-integrating samplers (Shah-Fairbank et al., 2011) and point-integrating samplers (Shah-Fairbank & Julien, 2015), respectively. Although analytically driven MEP-based methods are theoretically sound, their application range is limited to sand-bed streams (Shah-Fairbank & Julien, 2015; C.-Y. Yang & Julien, 2019).

Another solution for the total load estimation is to invert the relationship defined by the fraction of suspended load to total load $F_{sus} = Q_s/Q_t$. C.-Y. Yang and Julien (2019) investigated a large size of suspended sediment data in South Korean rivers using F_{sus} driven from SEMEP. Despite their plausible logic, the analyzed total loads were not from realistic bed load samples but from the SEMEP estimation values, and hence, limited. Turowski et al. (2010) furnished a profound investigation of F_{sus} using the measured data from various natural rivers. The new equation for short-term sediment in another study (Turowski et al., 2010) has the form $Q_b = AQ_s^B$, where A and B are the regression coefficients obtained without hydraulics-related factors . Accordingly, there is a need to design a field data-driven empirical model for F_{sus} that contains physical information.

F_{sus} can be readily estimated in a monitoring system using simple relationships, but a few factors should be considered. In general, the rating curves are fitted and implemented in real-time monitoring systems in the form $Q_t = AQ^B$, where Q is the cross-sectional flow discharge. In general, simple rating curves are inaccurate in unsteady flows, because a hysteresis loop is observed for the sediment load, similar to discharge-depth hydrographs (Gellis, 2013). However, the reason for using rating curves is that such hydraulic variables are easier to measure than sediment features. For example, the suspended sediment concentration and sample grain size, as required by MEP, are not easy to obtain in conventional discharge monitoring stations. Recently, the concentration is being alternatively measured at real-time discharge monitoring stations equipped with acoustic Doppler current profilers (ADCPs) (Noh et al., 2022). However, measuring the grain size distribution of the suspended sediment still depends on water sampling.

Under these circumstances, our goal is to suggest cost-effective empirical models to estimate F_{sus} and analyze the models. Prior to model derivation, data processing, including dimensional analysis, was conducted. Using recursive feature elimination for support vector regression (RFE-SVR), influential dimensionless variables for F_{sus} were identified. According to the SVR result, the two symbolic regression methods, Operon and multi-gene genetic programming, were utilized to deduce the relationships between the dimensionless variables in explicit forms. Clustering and sensitivity analyses were performed to unveil the underlying physics of the resultant equations and relevant datasets. This study was conducted under the following assumptions or restraints: (1) non-cohesive sediments and (2) exclusion of grain size of the suspended sediment.

2 Dimensional Analysis

First, to obtain reasonable dimensionless numbers for total sediment transport estimations, dimensionless numbers were deduced based on Buckingham's Pi theorem. The dimensionless variables examined in a previous study (Tayfur et al., 2013) were additionally referred to and rearranged to avoid duplications. Table 1 compiles the dimensionless variables presented in this study, where g is the gravitational acceleration; ρ_s and ρ_w are the densities of sediment and water, respectively; γ_s and γ_w are the specific weights of sediment and water, respectively; W is the channel width; h is the channel depth; U is the flow velocity; U_* is the shear velocity; S_0 is the channel slope; w_s is the falling velocity of sediment particles; d_{84}, d_{50}, and d_{16} are the sediment particle sizes of the 84%, 50%, and 16% of the material by weight, respectively; R_h is the hydraulic radius; ν is the kinematic viscosity of water; τ is the shear stress; β is the ratio of the turbulent mixing coefficient of sediment to the momentum exchange coefficient (assumed to be 1); κ is the von Karman coefficient; and Q_s and Q_b are the suspended- and bed-load sediment discharges.

The selection of appropriate input variables requires extensive sediment transport observations and analyses. Table 2 lists the published empirical equations for estimating the total loads and the dimensionless parameters of the equations. In the table, C_w

Table 1. Dimensionless variables related to sediment transport

Variables	Definitions	Variables	Definitions
$G_s = \frac{g\rho_s}{g\rho_w} = \frac{\gamma_s}{\gamma_w}$	Specific gravity	$\frac{W}{h}$	Channel width depth ratio
$\frac{U}{U_*} \approx \frac{U}{\sqrt{gR_hS_0}} \approx \frac{U}{\sqrt{ghS_0}}$	Friction factor	$\frac{US_0}{w_s}$	Dimensionless stream power
$Gr = \frac{1}{2}(\frac{d_{84}}{d_{50}} + \frac{d_{50}}{d_{16}})$	Gradation coefficient	$\sigma_g = (\frac{d_{84}}{d_{16}})^{1/2}$	The gradation of the sediment mixture
$d_* = d_{50}[\frac{g(G_s-1)}{\nu^2}]^{1/3}$	Dimensionless particle size	$\frac{R_h}{d_{50}} \approx \frac{h}{d_{50}}$	Dimensionless hydraulic radius
$Re_{d50} = \frac{Ud_{50}}{\nu}$	Particle Reynolds number	$Re_h = \frac{Uh}{\nu}$	Flow Reynolds number
$Re_* = \frac{U_*h}{\nu}$	Shear Reynolds number	$Re_{d*} = \frac{U_*d_{50}}{\nu}$	Particle shear Reynolds number
$Re_w = \frac{w_sd_{50}}{\nu}$	Falling particle Reynolds number	$Fr = \frac{U}{\sqrt{gh}}$	Froude number
$Fr_d = \frac{U}{\sqrt{g(G_s-1)d_{50}}}$	Particle Froude number	$Ro = \frac{w_s}{\beta\kappa U_*}$	Rouse number
$\tau_* = \frac{\tau}{g\rho_w(G_s-1)d_{50}} = \frac{U_*^2}{g(G_s-1)d_{50}}$	Shields number	$F_{sus} = \frac{Q_s}{Q_s+Q_b}$	Suspended-total sediment load fraction

and C_{ppm} denote the total sediment concentration by the sediment weight per total weight and parts per million units, respectively.

In improvemetns of the modified Einstein procedure (Colby & Hembree, 1954; Shah-Fairbank et al., 2011; Shah-Fairbank & Julien, 2015; C.-Y. Yang & Julien, 2019), U_*/w_s and h/d_{50} were considered governing factors related to the suspended and total loads. For example, Shah-Fairbank et al. (2011) demonstrated that U_*/w_s and h/d_{50} are the major factors determining the ratio of suspended to total sediment discharge and that U_*/w_s is more influential than h/d_{50}.

$$F_{sus}(Ro,h,d_s) = \frac{0.216\frac{E^{Ro-1}}{(1-E)^{Ro-1}}\{\ln(\frac{30h}{d_s})J_1' + J_2'\}}{1 + 0.216\frac{E^{Ro-1}}{(1-E)^{Ro-1}}\{\ln(\frac{30h}{d_s})J_1 + J_2\}} \tag{1}$$

In the above equation,

$$J_1 = \int_E^1 (\frac{1-z}{z})^R odz \tag{2}$$

and

$$J_2 = \int_E^1 \ln z(\frac{1-z}{z})^R odz \tag{3}$$

where E is the ratio of bed layer thickness to flow depth, which is commonly used in the form $2d_{50}/h$. For the integration of the measurable area, the corresponding integrals J_1' and J_2' can be computed by substituting E with $a = z_n/h$, where z_n is the minimum height of the suspended sediment sampler nozzle.

Although a few variables in Table 1 do not appear in Table 2, the following analyses embrace all possible dimensionless variables on their virtues. For example, W/h significantly influences the suspended to total load ratio (Edwards et al., 1999). W/h is a morphologically important factor resulting from stream bank stability, along with sinuosity and S_0 (D. L. Rosgen, 1994). Gr is also considered a particle size distribution indicator because of its apparent contributions (e.g., entrained suspended particle size (Van Rijn, 1993)).

3 Data

The analyses in this study require not only the integrated total sediment loads but also the suspended and bed loads with hydraulic variables. The target dataset includes data from the United states geological survey (USGS) report on the measurement of suspended and bed loads in 93 natural rivers (Williams & Rosgen, 1989). The targeted dataset is a natural river sediment load monitoring dataset based on field sampling that includes

Table 2. Empirical equations for total loads with dimensionless variables

References	Formulae	Dim.less parameters
Bagnold (1966)	$\frac{Q_t}{W} = q_t = q_b + q_s = \frac{\tau_0 U}{G_s - 1}(e_B + \frac{0.01U}{w_s})$, where $0.2 < e_b < 0.3$	$C = f(\frac{U}{w_s})$
Engelund and Hansen (1967)	$\frac{q_t}{\sqrt{(G_s-1)d_{50}^3}} = \frac{1}{C} 0.05 (t^*)^{2.5}$ or $C_w = 0.05(\frac{G_s}{G_s-1}) \frac{US_0}{\sqrt{(G_s-1)gd_{50}}} \frac{R_h S_0}{d_{50}(G_s-1)}$	$C = f(\frac{U}{U_*}, \frac{R_h}{d_{50}})$
Shen and Hung (1972)	$\log C_{ppm} = [-107,404.459 + 324,214.747Sh$ $-326,309.589Sh^2 + 109,503.872Sh^3]$ where, $Sh = (\frac{US_0^{0.57159}}{w_s^{0.31988}})^{0.00750189}$	$C = f(\frac{US_0}{w_s})$
Ackers and White (1973)	$C_w = c_{AW2} G_s (\frac{d_{50}}{R_h})(\frac{U}{U_*})^{c_{AW1}} (\frac{c_{AW5}}{c_{AW3}} - 1)^{c_{AW4}}$ $c_{AW5} = \frac{U_*^{c_{AW1}}}{\sqrt{(G_s-1)gd_{50}}} (\frac{U}{\sqrt{32}\log(10h/d_{50})})^{1-c_{AW1}}$ for $1.0 < d_* \leq 60.0$ $c_{AW1} = 1.0 - 0.56 \log d_*$ $c_{AW2} = 2.86 \log d_* - (\log d_*)^2 - 3.53$ $c_{AW3} = \frac{0.23}{\sqrt{d_*}} + 0.14$ $c_{AW4} = \frac{9.66}{d_*} + 1.34$ for $d_* > 60.0$, $c_{AW1} = 0$, $c_{AW2} = 0.025$, $c_{AW3} = 0.17$,$c_{AW4} = 1.50$	$C = f(\frac{U}{U_*}, \frac{R_h}{d_{50}},$ $\frac{U_*}{\sqrt{(G_s-1)gd_{50}}}, d_*)$
C. T. Yang (1979)	for sand, $C_{ppm} = 5.435 - 0.286 \log \frac{w_s d_{50}}{\nu} - 0.457 \log \frac{U_*}{w_s}$ $+(1.799 - 0.409 \log \frac{w_s d_{50}}{\nu} - 0.314 \log \frac{U_*}{w_s}) \log(\frac{US_0}{w_s} - \frac{U_c S_0}{w_s})$ for $1.2 < \frac{U_* d_{50}}{\nu} < 70.0$ $\frac{U_c}{w_s} = \frac{2.5}{\log(\frac{U_* d_{50}}{\nu}) - 0.06} + 0.66$ for $70 \leq \frac{U_* d_{50}}{\nu}$, $\frac{U_c}{w_s} = 2.05$	$C = f(\frac{US_0}{w_s}, \frac{U_*}{w_s}, \frac{w_s d_{50}}{\nu}, \frac{U_* d_{50}}{\nu}, S_0)$
Karim (1998)	$\frac{q_t}{\sqrt{(G_s-1)d_{50}^3}} = 0.00139(\frac{U}{\sqrt{(G_s-1)d_{50}}})^{2.97}(\frac{U_*}{w_s})^{1.47}$	$C = f(\frac{U}{\sqrt{(G_s-1)d_{50}}}, \frac{U_*}{w_s})$
Molinas and Wu (2001)	$C_{ppm} = \frac{1430(0.86+\sqrt{\Psi})\Psi^{1.5}}{0.016+\Psi}$ where, $\Psi = \frac{U^3}{(G_s-1)ghw_s(\log(h/d_{50}))^2}$	$C = f(\frac{U}{U_*}, \frac{U}{w_s}, \frac{h}{d_{50}})$
Tayfur et al. (2013)	$C_{ppm} = [0.00075(\frac{U_* d_{50}}{\nu})^{2.5047}(\frac{1}{d_*^3})^{0.2117}(\frac{R_h}{d_{50}})^{1.2405}$ $(\frac{q_t}{\sqrt{(G_s-1)d_{50}^3}})^{-0.3637}(\frac{U_*^2}{gd_{50}})^{0.7975}(\frac{U}{\sqrt{g(G_s-1)d_{50}}})^{0.9561}]$	$C = f(\frac{U_* d_{50}}{\nu}, d_*, \frac{R_h}{d_{50}},$ $\frac{q_t}{\sqrt{(G_s-1)d_{50}^3}}, \frac{U_*^2}{gd_{50}}, \frac{U}{\sqrt{g(G_s-1)d_{50}}})$
Okcu et al. (2016)	$C_{ppm} = 34.45 \frac{P^{3.239} J^{0.005}}{L^{0.066} R^{0.146}}$ where, $P = \frac{U}{\sqrt{(G_s-1)gd_{50}}}$ $J = \exp[(\ln S_0)^3]$ $L = \exp[(\ln(h/d_{50}))^2]$ $R = \frac{U_* d_{50}}{\nu}$	$C = f(\frac{U}{\sqrt{(G_s-1)d_{50}}}, S_0, \frac{h}{d_{50}}, \frac{U_* d_{50}}{\nu})$

sample analysis of both suspended and bed loads with hydraulic variable measurements. The input variables and calculated dimensionless numbers are summarized in Table 3.

The kinematic viscosity of water, $\nu = \mu/g$, was obtained based on the Vogel equation (Vogel, 1921), which is calculated as follows:

$$\mu = g\nu = \exp[-3.7188 + \frac{578.919}{-137.546 + T_K}], \tag{4}$$

where μ is the dynamic viscosity of water and T_K is the temperature in Kelvin. The coefficients from the above equation are obtained from the website of Dortmund Data Bank Software and Separation Technology (DDBST GmbH, n.d.).

The National Institute of Standards and Technology (Maryland, USA) adopts the model from Wagner and Pruß (2002) for density calculation, but it is known to be extremely complicated. Thus, all density-related variables were calculated using Equation

Table 3. Summary of the dataset (Nan rows excluded)

	Count	Mean	Std.	Min.	Max.
Q (cms)	1,957	2.26×10^{2}	5.15×10^{2}	7.00×10^{-3}	3.77×10^{3}
U (m/s)	1,721	1.05	6.41×10^{-1}	4.70×10^{-2}	3.40
W (m)	1,894	5.70×10^{1}	8.95×10^{1}	6.40×10^{-1}	5.18×10^{2}
H (m)	1,764	1.01	1.18	4.00×10^{-2}	5.80
S_0	650	7.39×10^{-3}	2.14×10^{-2}	9.30×10^{-5}	1.88×10^{-1}
u_* (m/s)	632	1.48×10^{-1}	8.51×10^{-2}	3.02×10^{-2}	6.37×10^{-1}
Temp. (°C)	1,026	9.92	5.19	5.00×10^{-1}	3.00×10^{1}
C_w (mg/l)	1,957	3.31×10^{2}	1.39×10^{3}	1.00	2.91×10^{4}
Q_s (kg/s)	1,957	1.81×10^{2}	7.68×10^{2}	2.50×10^{-5}	1.41×10^{4}
Q_b (kg/s)	1,928	7.75	2.32×10^{1}	3.20×10^{-7}	3.38×10^{2}
d_{16} (mm)	1,487	9.95×10^{-3}	1.39×10^{-2}	1.06×10^{-4}	9.04×10^{-2}
d_{50} (mm)	1,530	3.77×10^{-2}	4.07×10^{-2}	2.78×10^{-4}	2.16×10^{-1}
d_{65} (mm)	1,530	5.58×10^{-2}	5.78×10^{-2}	3.26×10^{-4}	2.89×10^{-1}
d_{84} (mm)	1,530	9.85×10^{-2}	1.02×10^{-1}	4.25×10^{-4}	4.46×10^{-1}
ν (m^2/s)	1,957	1.17×10^{-6}	2.00×10^{-7}	8.04×10^{-7}	1.71×10^{-6}
σ_g	1,487	5.23	4.66	1.46	2.37×10^{1}
Gr	1,487	8.09	1.12×10^{1}	1.46	5.99×10^{1}
F_{sus}	1,928	7.49×10^{-1}	2.69×10^{-1}	1.82×10^{-3}	1.00
W/h	1,755	4.74×10^{1}	5.63×10^{1}	3.03	6.32×10^{2}
H/d_{50}	1,409	3.59×10^{2}	1.10×10^{3}	5.10×10^{-1}	1.19×10^{4}
d_*	1,530	8.65×10^{2}	9.20×10^{2}	5.54	4.35×10^{3}
w_s	1,530	6.27×10^{-1}	3.86×10^{-1}	3.43×10^{-2}	1.76
US_0/w_s	389	1.03×10^{-2}	1.36×10^{-2}	9.20×10^{-5}	7.61×10^{-2}
U/u_*	589	9.58	4.57	2.06×10^{-1}	2.04×10^{1}
Re_h	1,720	1.35×10^{6}	2.21×10^{6}	6.16×10^{3}	1.60×10^{7}
Re_{d50}	1,366	2.96×10^{4}	3.12×10^{4}	1.33×10^{2}	2.05×10^{5}
Re_{d*}	431	5.66×10^{3}	1.02×10^{4}	1.05×10^{1}	6.07×10^{4}
Re_*	632	1.95×10^{5}	2.46×10^{5}	4.65×10^{3}	1.29×10^{6}
Re_w	1,530	3.31×10^{4}	5.13×10^{4}	6.69	2.70×10^{5}
Fr	1,720	3.97×10^{-1}	1.48×10^{-1}	3.00×10^{-2}	1.24
Fr_d	1,366	2.64	2.90	2.90×10^{-2}	2.39×10^{1}
U/w_s	1,366	3.05	3.85	3.08×10^{-2}	4.66×10^{1}
Ro	431	8.57	4.70	8.98×10^{-1}	2.33×10^{1}
$Shields$	431	2.25×10^{-1}	4.35×10^{-1}	9.74×10^{-3}	4.07

(5) (Civan, 2007), which was improved for both brevity and correctness.

$$\ln(1-\frac{\rho_w}{1065}) = 1.2538 - \frac{-1.4496*10^3}{T_C+175} + \frac{-1.2971*10^5}{(T_C+175)^2}(kg/m^3), \tag{5}$$

where T_C is the temperature in Celsius.

When the falling velocity w_s and Rouse number Ro are estimated, the median suspended grain size d_{50ss} is considered the characteristic grain size, particularly in the MEP. To ensure the applicability of the proposed models, we used d_{50} instead of d_{50ss}. For example, in remote sensing using aerial images for suspended sediment concentration, obtaining d_{50ss} for every monitoring event may not be reasonable. In the characteristic size percentile, the median bed material size d_{50} is used if the particle size percentile for a dimensionless variable is not explicitly expressed. Similarly, the falling velocity w_s was calculated using the following equation:

$$w_s = \frac{8\nu}{d_{50}}[(1 + 0.0139 d_*^3)^{1/2} - 1] \tag{6}$$

The shear velocity U_* was calculated using the water surface slope by approximating $U_* \sim \sqrt{ghS_0}$.

Equation 6 indicates that the falling velocity of the suspended particles is influenced by temperature because d_* depends on both the viscosity and density of water. If the temperature is greater than approximately 4 $°C$, both the density and viscosity decrease as the temperature increases. This results in an increase in ρ_s/ρ_w and a decrease in the viscous drag, which increases the falling velocity. Figure 1 shows the falling velocity changes owing to temperature and grain size variations. The y-axes in Figures 1(a) and (b) represent the dimensionless number $w_{s*} = w_s/\sqrt{(G_s-1)gd_s}$, which is the ratio of the falling velocity computed by Equation 6 to the terminal velocity under buoyancy force. Figure 1(c) shows the acceleration rate of the falling velocity by changing the temperature from 10 $°C$ to 25 $°C$. It must be noted that the falling velocity of the figure may differ from that of a real-world phenomenon because the silt or clay particles are likely to flocculate (Julien, 2010).

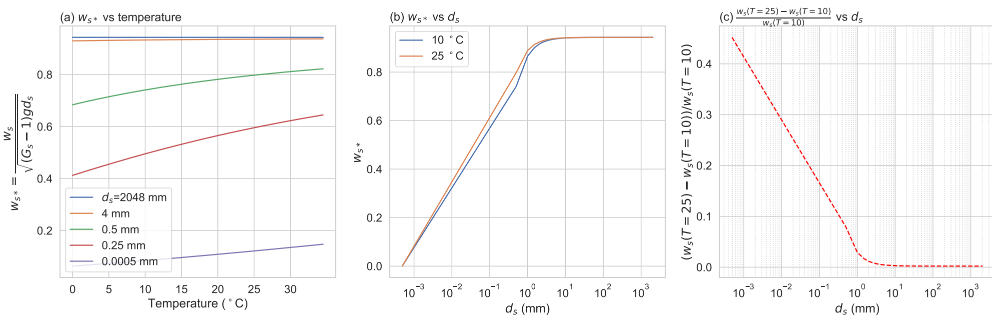

Figure 1. The temperature and grain size effects on the falling velocity: (a) w_s vs T; (b) w_s vs d_s; (c) $\frac{w_s(T=25)-w_s(T=10)}{w_s(T=25)}$ vs d_s

As shown in Figures 1(a) and (b), the effect of increasing falling velocity is insignificant when the grain size is larger than 4 mm. For larger particles (d_s >>4 mm), w_{s*} converges to 0.94. For particles smaller than 4 mm (fine gravel, sand, silt, and clay), the viscous drag is discernible, accompanying the temperature effect. The temperature effect is apparent in the range $10^{-3} < d_s < 4mm$. The gap between the orange and blue lines is maximized for sand-sized particles. As shown in Figure 1(c), the actual falling velocity of particles larger than fine gravel is insensitive to temperature variations. By contrast, $\frac{w_s(T=25)-w_s(T=10)}{w_s(T=25)}$ continues to increase as d_s decreases. Although the ratio of the gravity force to w_s appears to be insensitive to the temperature variation for small particles, the viscosity change due to temperature affects the actual falling velocity. For extremely fine sand, $d_s \approx 10^{-2}$ mm, the falling velocity changes by approximately 30%.

Overall, the analysis implied that the temperature effect should be considered for sand, silt, and clay particles. The average value of d_{50} of the dataset is 3.76 mm, and the inflection point is observed in Figure 1. Therefore, the dimensionless variables related to ρ_w and ν, such as w_s, are computed using Equations 4 and 5, respectively, considering the temperature effect.

4 Methodology

4.1 Tools for Empirical Model Development

In this study, three regression approaches were compared by developing an empirical model to estimate F_{sus}. The following subsections present the three different machine learning-based regression approaches, namely, SVR, MGGP, and Operon, used in the proposed F_{sus} estimation model.

4.1.1 Support Vector Regression (SVR)

SVR is a branch of a support vector machine (SVM) (Drucker et al., 1996). In the classification problem, SVM (or support vector classification) separates data classes from the decision boundary by maximizing the margin, which is the distance between two parallel hyperplanes expanded from the decision boundary. In contrast, SVR achieves regression by placing target data points within the fixed-width margin and constructing the flattest regression function possible. Figure 2 illustrates a schematic example of two SVR fitting cases to help understand the training rule of SVR.

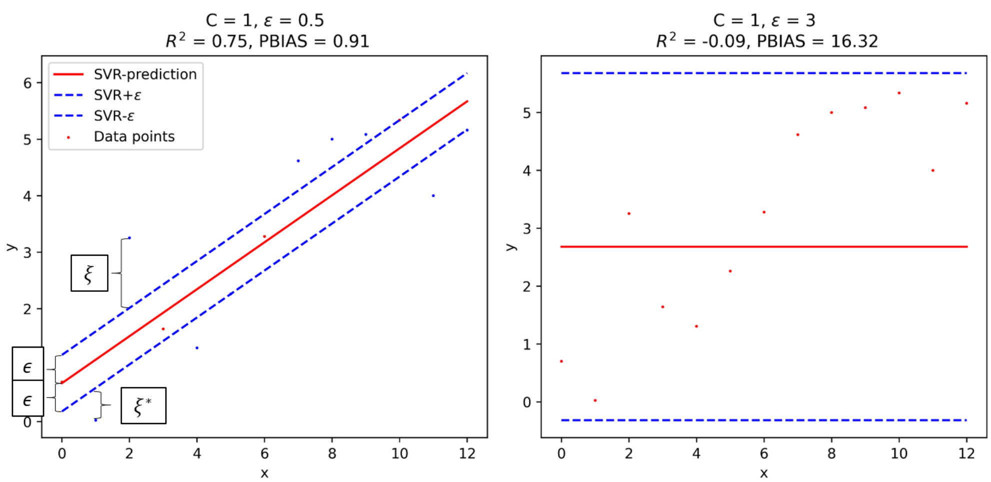

Figure 2. Schematic examples of the SVR training rule

In the figure, the tube consisting of the two blue dashed lines is the margin, and the width between the blue dashed lines is 2ϵ. In particular, soft margin SVR (C-SVR) is an advanced SVR model that allows the upper and lower offsets, ξ and ξ^*, respectively, from the margin demarcation. As shown in the figure, SVR attempts to include as many data points as possible within the margin, as indicated on the right-hand side. In the case of a sufficiently large ϵ that includes all data points, SVR flattens the regression curve, as shown in the right sub-figure.

C-SVR is trained by the optimization process of the following primal problem:

$$
\begin{aligned}
&\min_{\vec{w},b} && \tfrac{1}{2}||\vec{w}||^2 + C\sum_{i=1}^{n} F(\xi_i) + C_{SVR}\sum_{i=1}^{n} F(\xi_i^*) \\
&\text{subject to} && (\vec{w}^T\vec{x_i} + b) - y_i \le \epsilon + \xi_i \\
& && y_i - (\vec{w}^T\vec{x_i} + b) \le \epsilon + \xi_i^* \\
& && \xi_i, \xi_i^* \ge 0 \\
&\text{for} && i = 1, 2, ..., n,
\end{aligned}
\tag{7}
$$

where C_{SVR} is the regularization cost coefficient; $F(\xi)$ is the arbitrary cost function for ξ. SVR solves the Lagrangian dual problem in Equation 7. By setting the cost function l-1 $F(\xi) = \xi$, the Lagrangian dual problem can be set as follows:

$$\begin{aligned} \max_{\alpha,\alpha^*} \quad & -\tfrac{1}{2}\textstyle\sum_{i=1}^{n}\sum_{j=1}^{n}(\alpha_i-\alpha_i^*)(\alpha_j-\alpha_j^*)K(\vec{x}_i,\vec{x}_j) \\ & +\textstyle\sum_{i=1}^{n}(\alpha_i-\alpha_i^*)y_i-\sum_{i=1}^{n}(\alpha_i\epsilon+\alpha_i^*\epsilon^*) \\ \text{subject to} \quad & \textstyle\sum_{i=1}^{n}(\alpha_i-\alpha_i^*)=0 \\ & 0\le\alpha_i,\alpha_i^*\le C_{SVR} \\ & \text{for } i,j=1,...,n, \end{aligned} \tag{8}$$

$$\tag{9}$$

where α and α^* are Lagrangian multipliers and $K(x,x)$ is the kernel function. The kernel function maps the dot product $x_i^T x_j$ to a higher dimension such that SVR is likely to find the appropriate predictive function. When no kernel is applied, it is equal to the linear kernel, which has the functional form $K(x_i,x_j) = x_i^T x_j]$. Another popular kernel is the radial basis function (RBF) kernel, which is defined as:

$$K(x_i,x_j) = \exp[-\gamma||x_i - x_j||^2], \tag{10}$$

where γ is the inverse of the influence radius of the samples.

Notably, the above Lagrangian dual problem is a quadratic programming with respect to α and α^*, that is, the convex optimization rule is applicable. Furthermore, this problem satisfies the Karush-Kuhn-Tucker conditions, which guarantee that the solution to the dual problem coincides with that of the primal problem. Thus, SVR always yields a unique optimum solution when the target data and parameter combinations are provided. The fact that SVR always converges to a unique optimum solution benefits SVR. In contrast, neural networks are prone to converge to local optima because of parameter setting, learning rate, and noise in the data (Smola & Schölkopf, 2004).

4.1.2 Recursive Feature Elimination for SVM (RFE-SVR)

The extraction of the governing feature to express the empirical relationship was performed by recursive feature elimination for SVR (RFE-SVR). RFE-SVR is a feature-selection technique for the SVM problem suggested by Guyon et al. (2002). In RFE-SVR, the importance of each feature is updated according to the ranking criterion. For the linear SVM, the ranking criterion c_p is w_p^2, which is the p-th weight vector component corresponding to the p-th feature. As a generalization of nonlinear kernel applications, the ranking criterion of the p-th feature c_p can be computed as:

$$c_p = \frac{1}{2}|\sum_{i,j=1}^{N}(\alpha_i-\alpha_i^*)(\alpha_j-\alpha_j^*)K(x_j,x_j)) - \sum_{i,j=1}^{N}(\alpha_i-\alpha_i^*)(\alpha_j-\alpha_j^*)K(x_j^{(-p)},x_j^{(-p)}))|, \tag{11}$$

where $x_j^{(-p)}$ is x_j without the p-th feature. The update step eliminates the smallest feature importance c_p. Subsequently, SVM is trained using the input data of the reduced features. The training-elimination sequence continues until the features remain in the user-defined feature size.

In general, cross-validation (CV) is accompanied by RFE-SVR. CV provides information about the generalized performance of the model with minimized overfitting risk. The so-called K-fold CV method divides the entire dataset into K subsets and repeats the model fitting K times. For the i-th model fitting, the i-th subset is regarded as a test set, and the model is fitted to the remaining K-1 subsets. By repeating the training for each subset, the average test-set fitness score is considered the CV score. In RFE-SVR incorporated with CV, the algorithm evaluates the CV scores at every feature elimination step. CV signifies that the model with a certain parameter setting (e.g., input variable, hyperparameters of SVM) predicts not only the training set but also other datasets as well as the CV score.

4.1.3 Multi-Gene Genetic Programming (MGGP)

Genetic programming (GP), introduced by Koza (1992), is a symbolic regression technique that exploits the learning rule of the genetic algorithm (GA) in the empirical formulation. Unlike SVR, MGGP is a gray-box model because it produces explicit estimation equations where the machine finds the final equations (strictly, the regression function of SVR can be computed using α and α^*).

The individuals of the population are the genes in GP, as well as in GA. Every GP gene has a tree structure consisting of terminally connected branches. In the tree structure, functional operators, such as $+, -, \times, \div, \sqrt{\cdot}$, comprise a terminal, and the input variables are at the branches. Each gene becomes an equation by combining the variables according to the adjoint functional terminals, and regression performance measures are adopted as an objective function of the GP.

Because the GA concept is implemented in GP, the two representative GA operators, namely, mutation and crossover, are under the user-defined mutation and crossover probabilities. These GA operators modify the functional terminals of the population genes in every evolution of the selected gene. Mutation reproduces the offspring by changing the mathematical operators of the terminals. Two genes are required for the crossover operation. The crossover exchanges the terminals of the chosen genes to breed offspring. Examples of the two GP operations are illustrated in Figure 3, where the mutation and crossover are differentiated using colors.

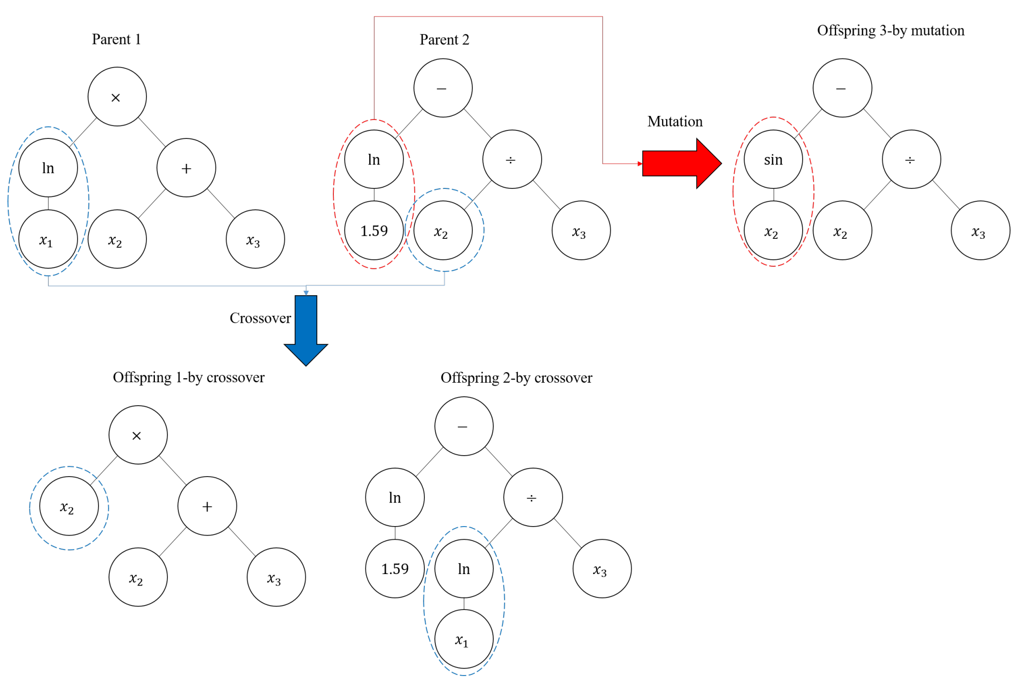

Figure 3. Examples of the GP operations

As a result of repeated evolutions, the population comprises various forms of equations. The best-fit equation in the last evolution is selected as the final product.

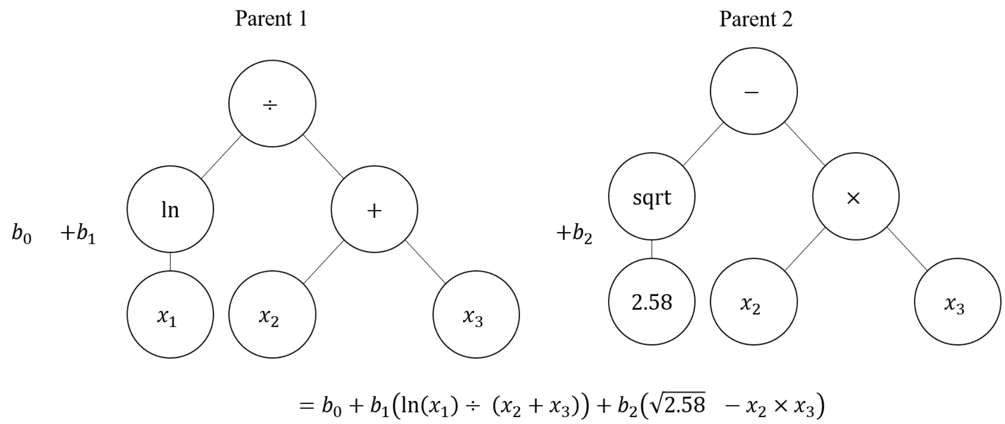

Figure 4. Example of MGGP formulation

MGGP is an advanced GP model. MGGP produces equations with multiple genes (terms of equations) for each solution (produced equation) to enhance variability without increasing the depth of the tree. Figure 4 shows an example of the gene expression of MGGP [tree depth = 3 and the number of trees = 2]. Additionally, GA operators operate in the MGGP. In MGGP, mutation and crossover events occur not only at the under-gene level but also at the gene-by-gene level. The former and latter operations are called high- and low-level operations for differentiation, respectively. For example, the high-level crossover exchanges the sub-genes of the two selected gene trees.

GA operations only formulate the structure of each formula in the population in MGGP. The regression coefficients (b_0, b_1, and b_2 in Figure 4) remain unknown. The least squares rule determines the regression coefficients. Finally, individuals in the population acquire a fully functional structure that can evaluate the target variable.

However, a simple model is more desirable than a complicated model that considers both overfitting and practicability. Thus, Pareto optimal solutions that satisfy both fitness and brevity are selected in the final step. In this regard, the MATLAB MGGP library genetic programming toolbox for the identification of physical systems (GPTIPS), which yields Pareto solutions, as proposed by Searson (2015), is utilized in this study for the MGGP model derivation. The other advantage of GPTIPS is that it provides multiple independent runs, and thus, the initialization effect decreases (refer to Searson (2015) for a more detailed explanation of MGGP).

4.1.4 Operon

The main question of the symbolic regression field is how to achieve advanced formulation by modifying the GP policy proposed by Koza, corresponding to MGGP adopting a high-level GA operation. Recently, La Cava et al. (2021) compared the performance of cutting-edge symbolic regression methods and black-box machine-learning models using several benchmark problems. The benchmark analysis includes the accuracy and equation complexity of each symbolic regression method. The benchmark test result indicated that Operon (Burlacu et al., 2020) was a Pareto front model that considered accuracy and model complexity and was a state-of-the-art method with respect to accuracy (La Cava et al., 2021).

Burlacu et al. (2020) suggested a new tree initialization algorithm to ensure the population diversity and implemented it to Operon. Operon determines the coefficients (such as b_0) of the symbolic inputs using a local search algorithm based on the nonlinear least squares method, which is supported by automatic differentiation. The local search fine tunes the coefficients of the individual equations, thereby increasing the accuracy of the final formulae. In addition, the encoding and offspring generation strategies of Operon reinforce strong parallelism and low memory demand.

4.2 Clustering

One of the main purposes of clustering analysis is to understand the underlying physical structures of inter-variable relationships (Jain, 2010). For this purpose, a clustering analysis was performed to inspect the detailed physical properties between F_{sus} and the input variables. The following subsections describe the clustering algorithms used in this study:

4.2.1 Self-Organizing Maps (SOMs)

Self-organizing maps (SOMs) are simple models that map a data space to a lower-dimensional manifold. The primal SOM was introduced by Kohonen (1990).

The update rule of the primal SOM involves pulling the best matching unit (BMU), which is the closest grid node, to a randomly selected data point and adjacent nodes. The batch learning SOM (Kohonen, 2012) learns the dataset in a statistical sense such that simultaneously updating BMUs for all data points is identical to updating each selected data point at least once. Let $\mathbf{m}_i$ be the i-th node and $\mathbf{x}_j$ be the j-th data point; then, the batch SOM finds the BMU of all data points according to the following equation:

$$c(\mathbf{x}_j) = \arg\min_i(d[\mathbf{x}_j, \mathbf{m}_i]), \tag{12}$$

$$\mathbf{m}_i = \frac{\sum_j \lambda(c(\mathbf{x}_j), i), \mathbf{x}_j)}{\sum_j \lambda(c(\mathbf{x}_j), i)}, \tag{13}$$

where, $\lambda(c(\mathbf{x}_j), i)$ is the neighborhood function describing the grid node-wise distance (e.g., $\lambda(c(\mathbf{x}_j), i) = \exp(c(\mathbf{x}_j) - i))$ and $d[\mathbf{x}_j, \mathbf{m}_i]$ is the Euclidian distance between $\mathbf{x}_j$ and $\mathbf{m}_i$].

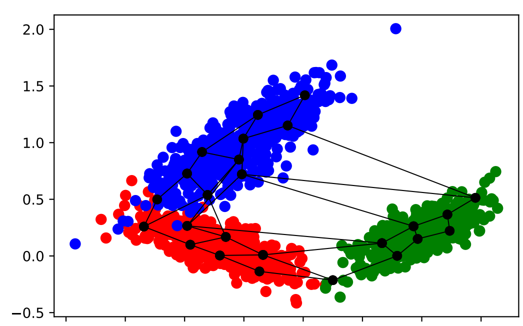

Figure 5. An example of 10 × 10 grid mapping of three Gaussian distributions by a planar self-organizing map

Figure 5 shows the 10×10 planar rectangular SOM grid mapped on random data points generated using three Gaussian distributions. SOM mimics the data distribution using the SOM map as black grids in Figure 5. Each grid point quantizes (summarizes) the data.

As the SOM map nodes are connected in a grid shape, the SOM map resembles the links between the quantized points. The advantageous feature of the SOM map is depicted in Figure 6. The hexagonal grid contours correspond to the x and y axes in Figure 5. The green dot cluster takes the place of the low y and the highest x. The upper right side of the SOM map projects the green cluster such that the grid nodes are bright and dark in 6 (a) and (b), respectively.

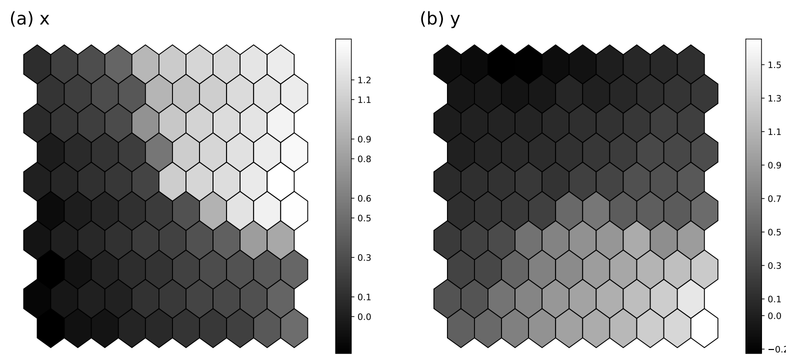

Figure 6. Component planes of the planar SOM depicted in Figure 5 for (a) x and (b) y

The mapping quality of the SOM can be checked using the topological error (TE) (Kiviluoto, 1996) and quantization error (QE) (Kohonen, 2012).

$$QE = \frac{1}{n}\sum_{j=1}^{n} ||x_j - w_{k^*l^*}|| \tag{14}$$

$$TE = \frac{1}{n}\sum_{j=1}^{n} u(x_j), \text{ where } \begin{cases} 1, \text{ first- and second-winning nodes non-adjacent} \\ 0, \text{ otherwise} \end{cases} \tag{15}$$

Here, $w_{k^*l^*}$ is the winning node corresponding to the j-th data point, x_j.

4.2.2 Gaussian Mixture Model (GMM)

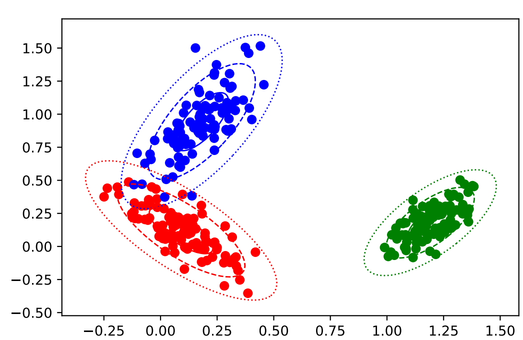

Figure 7. GMM mapping example on an arbitrary two-dimensional dataset ($K = 3$)

In natural cases, many datasets have statistical distributions. The Gaussian mixture model (GMM) assumes the data distribution as a mixture of K multi-variate Gaussian distributions, which is represented as

$$\mathcal{N}(x|\nu, \Sigma) = \frac{1}{(2\pi)^{D/2}} \frac{1}{|\Sigma|^{1/2}} \exp(-\frac{1}{2}(x-\boldsymbol{\mu})^T \boldsymbol{\Sigma}^{-1}(x-\boldsymbol{\mu})), \tag{16}$$

where x denotes the input data point, $\boldsymbol{\Sigma}$ denotes the covariance matrix, D denotes the number of dimensions, and $\boldsymbol{\mu}$ denotes the mean matrix. Figure 7 depicts how the three Gaussian distributions are mapped using GMM. By mapping data space into several Gaussian superpositions according to weight, probabilities of the data points for each Gaussian can be calculated. Let τ_k be the k-th Gaussian weight on the Gaussian mixture and μ_k and σ_k be the mean and covariance matrices, respectively; then, the probability density function of the trained GMM is calculated using Equation 17.

$$p(x) = \sum_{k=1}^{K} \tau_k \mathcal{N}(x|\boldsymbol{\mu}_k \boldsymbol{\Sigma}_k) \tag{17}$$

The probability of certain data can be viewed as the membership of K clusters.

The most common method used for training the GMM is the expectation-maximization (EM) algorithm (Dempster et al., 1977). The EM algorithm repeats the expectation and maximization steps until it converges with the log-likelihood objective function. In the expectation step, it calculates the membership of the data points in k-th Gaussian distribution according to the following equation:

$$\gamma(z_k) = p(z_k = 1|x) \equiv \frac{p(z_k = 1)p(x|z_k = 1)}{\sum_{j=1}^{K} p(z_j = 1)p(x|z_j = 1)} = \frac{\tau_k \mathcal{N}(x|\boldsymbol{\mu_k}, \boldsymbol{\Sigma_k})}{\sum_{j=1}^{K} \tau_j \mathcal{N}(x|\boldsymbol{\mu_j}, \boldsymbol{\Sigma_j})} \tag{18}$$

This step maximizes the log-likelihood of the Gaussian mixture. Once the $\gamma(z_k)$ values are obtained, the maximization step updates the parameters μ, Σ, and τ as follows:

$$N_k = \sum_{n=1}^{N} \gamma(z_{nk}) = \sum_{n=1}^{N} [\sum_{j} \tau_j \mathcal{N}(x_n|\boldsymbol{\mu}_j, \boldsymbol{\Sigma}_j)] \tag{19}$$

$$\boldsymbol{\mu}_k = \frac{1}{N_k} \sum_{n=1}^{N} \gamma(z_{nk}) x_n \tag{20}$$

$$\boldsymbol{\Sigma}_k = \frac{1}{N_k} \sum_{n=1}^{N} \gamma(z_{nk})(x_n - \boldsymbol{\mu}_k)(x_n - \boldsymbol{\mu}_k)^T \tag{21}$$

$$\tau_k = \frac{N_k}{N} \tag{22}$$

Here, N is the quantity of data.

A detailed derivation of Equations 18 – 22 can be found in Bishop (2006).

The fitness of the GMM can be evaluated using model criteria. The Akaike information criterion (AIC) (Akaike, 1974) and Bayesian information criterion (BIC) (Schwarz, 1978) are popular examples of GMM fitness measures. AIC and BIC are defined by Equations (23) and (24), respectively.

$$AIC = -2LL + 2N_p, \tag{23}$$

$$BIC = -2LL + N_p log(n)., \tag{24}$$

where LL is the log-likelihood of the fitted model and N_p is the number of parameters of the fitted model. A model with a small AIC and BIC is considered good.

4.2.3 SOM-GMM

The two-stage clustering method is commonly used to apply SOM by incorporating an additional clustering approach. In general, a trained SOM network is further divided using K-means (Li et al., 2018; Noh et al., 2021) or hierarchical clustering methods (Alvarez-Guerra et al., 2008; Kim et al., 2020). K-means clustering is a more intuitive and simpler model than other models, but it has certain disadvantages because of the assumption that the data points are distributed in spherical clusters. This assumption can lead to misclassification when non-spherically distributed data are used. Moreover, K-means is a hard clustering method that assigns one label to one data point; therefore, it is not appropriate to manipulate datasets when data regions of different classes overlap (Heil et al., 2019). This hard separation feature renders K-means sensitive to noise or outliers (Jain, 2010; Oyelade et al., 2016). A fuzzy c-means clustering (FCM) was introduced by Bezdek et al. (1984) as an alternative to overcome the problem of hard division by fuzzifying K-means directly. However, FCM is limited to hyperspherical clustering.

However, GMM assumes a fuzzy mixture of multi-variate Gaussians with varying cross-correlations, which is an advantage of GMM over K means and FCM. From another perspective, the expectation of K-means can be reproduced when the user sets the covariance matrix of GMM to be spherical (i.e., $\mathbf{\Sigma}_k = \sigma_k \boldsymbol{I}$). These characteristics of GMM make it more reliable than K-means in data classification in general. Regime shifts of the sediment transport mechanism in natural rivers might not be clearly divided and spherically distributed, but rather composed of thin ellipses. The Gaussian shape mapping rule of GMM that allows cross-correlation is advantageous for summarizing the sediment transport dataset. Therefore, GMM was selected as the secondary clustering method in this study. Hereafter, the two-stage clustering algorithm using SOM and GMM is referred to as SOM-GMM.

Two challenges of SOM-GMM must be considered: (1) the prerequisite of the predefined number of clusters K (and grid size $p \times q$) and (2) local optima followed by initialization. Different strategies were applied at each stage to address these challenges.

For the SOM stage, the grid size was determined according to the relationship $p \times q = 5\sqrt{n}$ (Vesanto et al., 2000). The location of each grid point, comprising a two-dimensional grid, was initialized by linearly spanning the grid over the two largest principal components following the principal component analysis (PCA) of the target dataset (Kohonen, 2012, 2013). This PCA-based grid initialization strategy always yields the same training results unless the training epochs and dataset change. To optimize the SOM training, the training epoch was optimized, minimizing both QE and TE (Equations (14) and (15)).

The final two-stage GMM partitioning result was selected using an iterative method that was similar to a method used previously (Noh et al., 2021). The GMM was essentially trained over the possible number of clusters K. Because GMM is prone to converge to the local optimum solution depending on the initial state, it is iteratively retrained for each K. For example, the SOM-GMM procedure runs 200 times when the possible K values are in the range of 2– 11, and 20 independent iterations are specified. AIC and BIC can be computed such that the clustering quality can be evaluated for every iteration. Finally, the case with the minimum AIC+BIC was selected as the best clustering result produced by the SOM-GMM procedure.

5 Results

5.1 GRID-RFE-SVR

For SVR parameter determination, we tuned the kernels and other parameters, such as C_{svr}, γ, and ϵ. Because the field sediment measurement data are accompanied by noise owing to various sources of uncertainties, it is important to allow soft margin SVM and reasonably determine noise regulation parameters (C_{svr} and ϵ) for an acceptable prediction of F_{sus}. Considering noise and overfitting, we tuned the parameters by grid searching using a cross-validation (grid-CV) approach. Table 4 lists the hyperparameter nominee grid points.

Sun et al. (2021) investigated SVR using the grid-CV by varying the possible hyperparameter ranges and steps. Their parameter ranges were $[2^{-8}, 2^{8}]$ and $[2^{-6}, 2^{6}]$, and their optimal solutions were: $C_{svr} = 4$ 16 and $\gamma = 0.004$ 0.008. Based on these observations, the parameter range basis of $[2^{-6}, 2^{6}]$ was selected. The upper limit of C_{svr} was extended to 2^{10} because C_{svr} could reach 900 (Ma et al., 2015). The ϵ-insensitive SVR does not impose a fitting penalty on the data points within ϵ. Accordingly, the grid range of ϵ is $[2^{-6}, 2^{3}]$ that includes the possible maximum value of $10^{F_{sus}} = 10$. Additionally, 0.001 was added.

Table 4. Tested hyperparameter grid for the GRID-RFE-CV

Hyperparameters	Values
ϵ	$10^{-3}, \{2^{-i} \mid i = [-6, 3]$ and $i \in \mathbf{I}\}$
C_{svr}	$\{2^{-i} \mid i = [-6, 10]$ and $i \in \mathbf{I}\}$
γ	$\{2^{-i} \mid i = [-6, 6]$ and $i \in \mathbf{I}\}$

In each hyperparameter combination of the grid-CV sequence, RFE-SVR was additionally performed, hereafter referred to as GRID-RFE-CV. In this GRID-RFE-CV system, the user can determine the hyperparameter values and input variables of the model with a generalized capability, supported by the cross-validation score.

All the dimensionless variables discussed in Section 2 were nominated to GRID-RFE-CV. To check the variable scaling effect of SVR fitting, the target variable F_{sus} and dimensionless input variables were scaled. In addition to F_{sus} without scaling, the scaling cases included logarithmic scaling ($log(F_{sus})$).

Table 5 presents the GRID-RFE-CV results for all the cases. The first and second numbers of the case names are distinguished by the input variables and F_{sus}, respectively. To compare the model performances, three criteria were evaluated, namely, the mean squared error (MSE), percent bias (PBIAS), and coefficient of determination R^2. The performance criteria in Table 5 can be defined as follows:

$$MSE = \frac{\sum_{i=1}^{n}(Y_{i,(obs)} - Y_{i,(est)})^2}{n}, \tag{25}$$

$$PBIAS = \frac{100}{n}\sum_{i=1}^{n}\frac{Y_{i,(est)} - Y_{i,(obs)}}{Y_{i,(obs)}}, \tag{26}$$

$$R^2 = \frac{\sum_{i=1}^{n}(Y_{i,(obs)} - Y_{i,(est)})^2}{\sum_{i=1}^{n}(Y_{i,(obs)} - \overline{Y_{(obs)}})^2}, \tag{27}$$

where $Y_{i,(obs)}$ and $Y_{i,(est)}$ are the observed and estimated values, respectively, and $\overline{Y_{(obs)}}$ is the mean observed value. Both MSE and R^2 describe the erraticity of the model. The former reflects the scale of the error, whereas the latter focuses on model predictability compared to lumped mean prediction. PBIAS is a useful indicator of over or underestimation of signs (+ or -). In addition, PBIAS measures errors corresponding to each data, whereas MSE and R^2 provide data-lumped error information.

The performance criteria values define the best variable model from GRID-RFE-CV. Once the best model is determined, SVR is refitted to the entire dataset using the best parameter and variable settings. In Table 5, the performance of the refitted model is denoted by MSE, PBIAS, and R^2. R^2-CV indicates the corresponding average test score in the cross-validation step. The overall ability of the model to predict F_{sus} and generalized predictability can be assessed using the data-driven criteria (MSE, PBIAS, and R^2) and R^2-CV, respectively.

Table 5. The condition of each case and the best model results from GRID-RFE-CV

Case	F_{sus}	Inputs	MSE	PBIAS	R^2	R^2-CV	Best variables
C11	F_{sus}	X	0.022	-0.553	0.730	0.578	W/h,d_*,Re_h,Fr_d,Re_w
C12	$\log(F_{sus})$	X	0.070	0.838	0.753	0.569	W/h,d_*,Re_h,Fr_d,Re_w
C13	$10^{F_{sus}}$	X	0.030	11.719	0.610	0.576	US_0/w_s,U/u_*,Re_h,Re_w,Gr
C21	F_{sus}	log(X)	0.024	-0.247	0.709	0.580	Re_h,Fr,Fr_d
C22	$\log(F_{sus})$	log(X)	0.074	0.756	0.740	0.578	Re_h,Fr,Fr_d
C23	$10^{F_{sus}}$	log(X)	0.031	14.018	0.600	0.583	H/d_{50},Re_h,Fr_d

In the cases where the input variables are not scaled, all the performance criteria support C11. In particular, the R^2-CV of C11 is 0.578, which is the best among C11, C12, and C13. Although the R^2 score of C12 is superior to C11 and C13, the MSE and PBIAS of C11 are better than those of C12. In particular, the MSE values of C11 are less than one-third of that of C12. R^2 of C12 is larger than that of C11 but less generalized. For the less generalized model, the new out-of-the-data predictability may be poor compared to the generalized model. Thus, C11 proves to be the best case among the cases without input-variable scaling.

The logarithmic scale of the input variables produces a similar trend to the scaling of F_{sus}. For instance, C21 in F_{sus} exhibits the lowest PBIAS and MSE for no scaling, and the $log(F_{sus})$ scaling case shows a good R^2 score but a lower R^2-CV. R^2-CV of C23 is slightly larger than that of the other cases, but R^2 of the refitted model is the least satisfactory value among all the tested cases. Therefore, using the C21 model is reasonable for logarithmic input scaling.

Considering the four performance measures, deriving the SVR models without F_{sus} scaling is preferable. The surviving input variables differ depending on whether the input variables are scaled. but they are independent of the F_{sus} scaling. The effective input variables are revealed from the frequencies of the surviving variables, as presented in Table 5. W/h, d_*, Re_h, Fr_d, and Re_w survived when the input variables were not scaled, whereas Re_h, Fr, and Fr_d survived for C21, C22, and C23. Notably, Re_h and Fr_d were the two most frequent features. Re_h survived for all cases, and Fr_d was excluded for C13. The survival frequency clearly shows the contributions of Re_h and Fr_d to F_{sus}.

Two different SVR models were derived based on GRID-RFE-CV analysis. The two SVR models use five and three surviving variables in C11 and C21, respectively. The names of the models are distinguished by the number of input variables, namely, SVR5 and SVR3. The optimal hyperparameter settings for the SVR models are set as follows: SVR3 -[kernel: RBF, $C_{svr} = 1$, $\gamma = 4$, $\epsilon = 0.125$], and SVR5 -[kernel: RBF, $C_{svr} = 1$, $\gamma = 8$, $\epsilon =$

0.0625]. The values are the same as the optimal hyperparameter settings obtained from the grid search.

5.2 Explicit Equations

Although crucial features for F_{sus} were identified by RFE-SVR with acceptable accuracy, the functional relationship remained hidden. The following subsection presents how the input variables interact with the help of explicit expressions, aided by symbolic regression. Cutting-edge machine-learning methods, MGGP and Operon, were used to identify the underlying sediment transport physics in F_{sus}. The analysis continues with clustering and sensitivity analyses.

5.2.1 MGGP

Formulation using MGGP requires certain parameter settings. The parameters that can be tuned in MGGP consist of formula shape and genetic algorithm parameters. Determining the functional form depends on the mathematical operator used in MGGP. In addition to the arithmetic operations, exponential operators (power, tanh, log, and exp) were included. A formula can be generated under the function set and formula size parameter (maximum gene number and tree depth)using the genetic algorithm parameters. Thus, the population size and generations must be sufficiently large to appropriately examine the functional structure to obtain reasonable results. However, increasing the population size and generation is not a solution. Essentially, genetic algorithms lose solution diversity, converging individual solutions to a certain form for one sequence. Therefore, in this step, the population using the number of runs was reset to 200. However, an increase in shuffling within the genetic algorithm operators (crossover, mutation, and replacement) results in a trade-off between population diversity and dismantling of the population. The determined MGGP parameter settings are presented in Table 6.

MGGP provides Pareto optimal equations; thus, several optional equations can be selected as the final product. In this study, the best models with respect to the test set scores were chosen and compared. For the perceptibility of the explicit models, a few terms such as A_{M3} were included as separate expressions. The replaced symbols use A, B, C, D, and E with the subscripts denoting the symbolic regression method. For example, $M3$ is the three-variable MGGP model and $O5$ is the five-variable Operon model.

The three-variable MGGP model (MGGP3) was derived using Equations (28) – (29).

$$F_{sus} = 0.406\, e^{A_{M3}} - 1.97\, e^{-Re_h} - 0.779\, e^{{Fr_d}^2} + 0.779\, e^{-{Re_h}^3} + 1.45\, {Fr_d}^2 + 1.77 \tag{28}$$

$$A_{M3} = e^{-6\, Fr_d - 3\, Re_h} - Fr^2\, {Re_h}^3 \tag{29}$$

Fr appears in only once in Equation (29), with the accompanying Re_h. For Fr, F_{sus} decreases with an increase in Fr. In addition, Re_h with Fr appears to affect the scaling of Fr in the last term of Equation (32).

The MGGP5 model has a more complicated structure than MGGP3. Equations (30) – (32) are mathematical expressions for MGGP5.

$$F_{sus} = 0.365\, e^{A_{M5}} - 0.549\, d_* - 0.0521(e^{B_{M5}} + Re_h + \sqrt{(\frac{W}{h})^{d_*}}) + 0.222\, \frac{W}{h}\, d_* + 0.708 \tag{30}$$

$$A_{M5} = \frac{e^{-\frac{\tanh(Re_h)}{Re_h + d_*}}}{\tanh\left((e^{-Re_w})^{Re_h\, d_*}\right)} \tag{31}$$

Table 6. MGGP parameter settings

Parameter	Settings
Mathematical operators	$+, -, \times, \div, \sqrt{}$, square, cube, exp, tanh, log, power
Population size	500
Number of generations	500
Runs	200
Maximum number of genes	4
Maximum tree depth	6
Tournament size	15
Elitism	0.15 of population
Crossover events	0.84
High-/low-level crossover	0.2 / 0.8
Mutation events	0.14
Sub-tree mutation	0.9
Replacing input terminalwith another random terminal	0.05

$$B_{M5} = 3\, e^{-Re_h} \tag{32}$$

In the above formulation, MGGP considers all five surviving variables (W/h, d_*, Re_h, Fr_d, and Re_w). However, the resultant equation does not contain Fr_d, which is related to the grain size-flow interaction. Instead, d_* and Re_w are included. Notably, composite effects of W/h and d_* are observed.

5.2.2 Operon

The low computational cost and accuracy of Operon enable heuristic input parameter tuning with less effort compared to MGGP. Hence, in this study, the input parameters of Operon were determined by a grid search using multiple Operon runs. The test parameter grid was identical to that in a previous study (La Cava et al., 2021).

Operon3 (Equations 33 – 38) requires three variables but is the most complicated among the explicit formulations proposed in this study.

$$F_{sus} = \frac{1.012\ (2.616\, Re_h - 11.552\, Fr + A_{O3} - B_{O3} + C_{O3})}{\sqrt{(0.711\, Re_h - 11.392\, Fr + D_{O3})^2 + 1}} - 0.009 \tag{33}$$

$$A_{O3} = \frac{20.192\, Fr - 1.331}{\sqrt{(7.505\, Re_h - 0.567\, Fr + E_{O3} - 0.04)^2 + 1}} \tag{34}$$

$$E_{O3} = \frac{45.229\, Fr_d}{\sqrt{\frac{11.916304\, Fr^2}{387.893025\, {Re_h}^2 + 1} + 1}} \tag{35}$$

$$B_{O3} = \frac{(3.364\, Fr - 1.587)}{\sqrt{8330.395441\, {Re_h}^2 + 1}} \tag{36}$$

$$C_{O3} = (3421.821\,Fr_d + 0.005)\,(0.075\,Re_h + 0.004\,Fr + 0.005) \tag{37}$$

$$D_{O3} = (0.057\,Re_h + 0.015)\,(9.269\,Re_h + 3739.117\,Fr_d + 31.422) \tag{38}$$

The five-variable Operon model was produced using the following equations:

$$F_{sus} = 0.499\,\frac{W}{h} - A_{O5} - B_{O5} + 2.622 \tag{39}$$

$$A_{O5} = \frac{\left(2.878\,\frac{W}{h} + 1.345\,d_* + 2.235\,Fr_d\right)}{\sqrt{5670.843025\,{Re_h}^2 + 1}} \tag{40}$$

$$B_{O5} = \frac{\left(27.784\,Re_h - 0.657\,d_* - 2.446\,Fr_d + \frac{0.563}{\sqrt{38808.212\,{Re_w}^2+1}} + 1.331\right)}{\sqrt{288.388324\,{Re_h}^2 + 1}} \tag{41}$$

Operon5 uses five complete variable sets, including Fr_d, which are not included in MGGP5.

The empirical equations produced by Operon have a complicated structure but are accurate. The formulations of MGGP3 and MGGP5 show dependence on $exp[Re_h]$, resulting in the potential for computational overhead. However, the equations derived using Operon consist of multi-fractional expressions.

Nonlinear least-squares local optimization coefficient tuning distinguishes Operon from the MGGP models. For example, some terms in MGGP models share coefficients (the third and fourth terms in Equation (28)). Each term in the Operon model has a particular fine-tuned coefficient value. This coefficient tuning increases the predictability but lengthens the equation. The above Operon models were additionally rearranged, and the coefficient values were truncated to the sixth decimal place for simplicity.

5.3 Model Performances

Table 7 shows the F_{sus} estimation performance of the derived models. Similar to that in Table 5, MSE and PBIAS indicate the scores evaluated using the entire dataset. R^2-train and R^2-test are the training- and test-set scores, respectively, divided by the ratio 7:3. Because SVR3 and SVR5 were refitted using the entire dataset, the CV test scores were listed.

Table 7. Performance measure of the empirical equations in estimation of F_{sus}

	MSE	PBIAS	R^2-training	R^2-test	R^2-all
SVR3	0.0375	-0.8462		CV-0.3928	0.5352
SVR5	0.0184	0.2783		CV-0.5209	0.7722
MGGP3	0.0587	0.1879	0.2619	0.3046	0.2720
MGGP5	0.0552	-0.5808	0.3273	0.2822	0.3161
Operon3	0.0445	-0.6262	0.4743	0.3723	0.4488
Operon5	0.0458	1.0820	0.4302	0.4076	0.4317

Every proposed model may estimate a value outside of the range [0,1]. Because values with $F_{sus} > 1$ or negative values are physically incorrect, all estimated values over one are corrected to 1. The negative values are adjusted to 10^{-4} to prevent infinite total load values when $Q_t = Q_s/0 = \infty$. These physical limitations must be applied to practical applications of these models.

In terms of MSE, the two SVR-driven models were superior to other symbolic regression models. Operon3 and Operon 5 were next in terms of performance. The MGGP models showed the most significant dispersion compared with the others. The MSE of the five-variable model was two times smaller than that of the three-variable model for SVR. In contrast, Operon3, with MSE = 0.0445, was slightly superior to Operon5, with MSE = 0.0458. SVR5 estimated F_{sus} accurately with the smallest MSE, 0.0184, which was 2 and 2.4 times lesser than that of SVR3 and Operon3, respectively.

A distinct result of PBIAS is the suitability of MGGP3, which has the smallest absolute PBIAS. MGGP3 yielded the lowest absolute value of PBIAS, and SVR5 yielded the second lowest value. On average, Operon5 overestimated F_{sus} by a factor of two with PBIAS > 1. In contrast, SVR3 (PBIAS=-0.8462) underestimated F_{sus}, compelling a large contribution of bed loads.

SVR5 showed excellent accuracy in terms of R^2-test (0.5209) and R^2-all (0.7722). R^2-all values of SVR3 ranked second, but the value of R^2-test (0.3928) for SVR3 was slightly lower than that for Operon5 (0.4076). Operon3 was superior in MSE, PBIAS, and R^2-all to Operon5. Upon comparing Operon3 and Operon5, a high score in R^2-training and low score in the test set was observed for Operon3, implying a possible over-fitting of the training set. The two MGGP-driven models showed low R^2 values for all the data combinations. MGGP5 predicted the training set better than MGGP3; however, MGGP3 was more accurate in the test set.

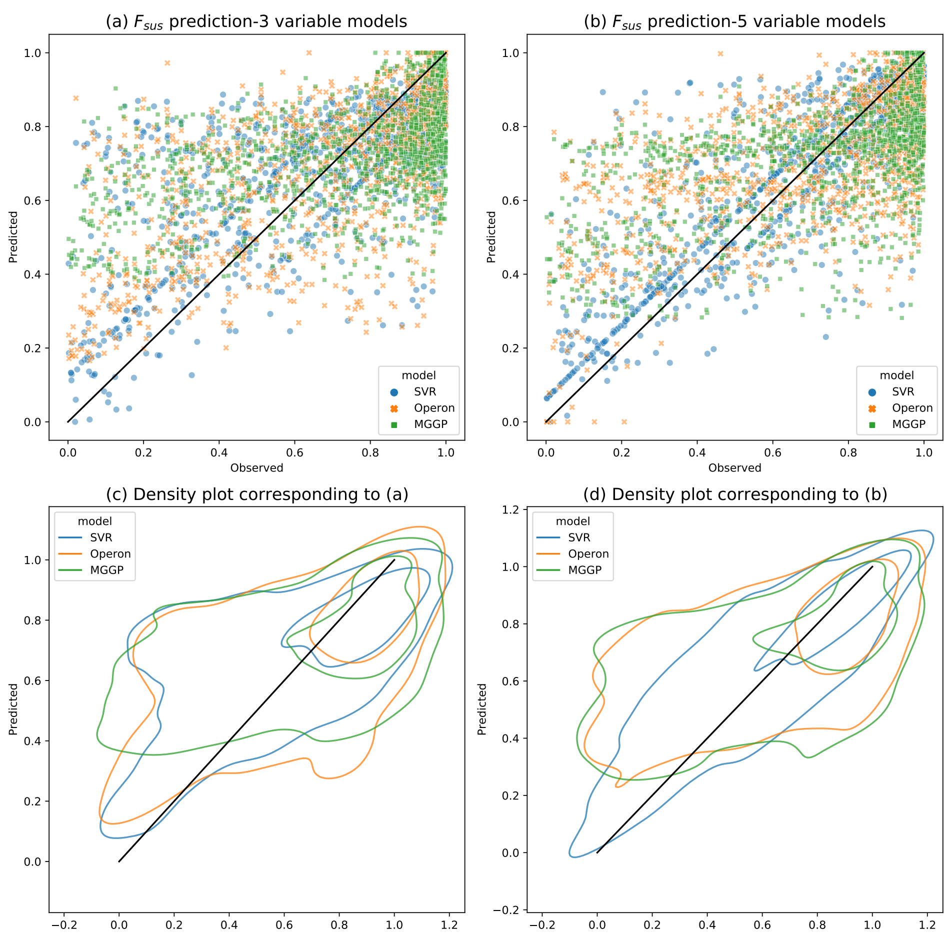

Figure 8. Scatter plots for F_{sus} estimation

Figure 8 shows the estimation results of the six models as scatter and density plots. The figures on the left-hand side are for the three-variable models, and those on the right-hand side are for the five-variable models; the symbols represent the derivation methods. The black lines are the 1:1 lines of perfect estimations.

In the scatter plots, almost all markers are under the 1:1 line when F_{sus} is close to 1, while for low values, the markers are over the 1:1 line . All models appear to fit, centering approximately on the average of F_{sus}, 0.749. In addition, the overestimation of the lower values establishes the lower limit barriers in cases of Operon3, MGGP3, and MGGP5.

Notably, in Figures 8(a) and (b) the blue dots are aligned in the vicinity of the 1:1 line. This alignment is derived from the unique characteristic that SVR, which is insensitive to ϵ, does not charge penalties to ϵ tube within the data points. In other expressions, the points aligned along the boundary of the ϵ tube represent support vectors. The reason why the recognized tube sizes are different in Figures 8(a) and (b) is that the ϵ values differ for SVR3 (0.0625) and SVR5 (0.03125).

Additionally, two density plots were drawn for perceptibility. The two circles indicate the two density levels for each color, which are the same as those in the scatter plots. The closer to the 1:1 line and thinner, the more accurate is the model. Most F_{sus} observations are distributed in the range from 0.75 to 1, and the inner circles cover the range. Using the two distinguished circles, the performance at large and low values can be resolved.

As proven above, SVR5 exhibits the best performance among the proposed models, with the thinnest inner and outer circles. The left orange lines representing Operon3 appear at a comparable level to SVR3, which is the best-performing three-variable model. Although the outer line of SVR3 is the thinnest between the models on the left-hand side for $F_{sus} < 0.75$, the three-variable models present underestimation for large values, as evidenced by the inner circle. Contrary to the high predictability of Operon3, Operon5 does not predict well, covering a range similar to that of MGGP5.

6 Discussion

6.1 Clustering Analysis

A clustering analysis was performed to simplify the underlying pattern of the sediment transport. Prior to applying the clustering algorithm, the correlations between the derived dimensionless variables were inspected. Figure 9 presents a correlation heat map for the dimensionless variables. For F_{sus}, which is the key parameter of this study, six variables were filtered based on the condition that the absolute values of the Pearson correlation coefficient were greater than 0.5. The six selected variables that significantly correlate with F_{sus} are W/h, US_0/w_s, U/U_*, H/d_{50}, Re_h, and Fr_d, which are also marked in the correlation map. Notably, the variables with a maximum-to-minimum ratio higher than 10^4 were analyzed on a logarithmic scale.

The data length was 1,346, and the corresponding optimal SOM map size was calculated as $5\sqrt{1346} = 183.5$. Thus, the grid size of the SOM was set as $14 \times 13 = 182$. The test range of the epochs of the SOM and the number of GMM clusters K were [0,1000] and [2, 10], respectively.

The QE-TE test results are shown in Figure 10. Both QE and TE rebounded after 300 epochs of the SOM update. To ensure the lowest QE and TE, GMM was performed after fixing the SOM to 250 epochs.

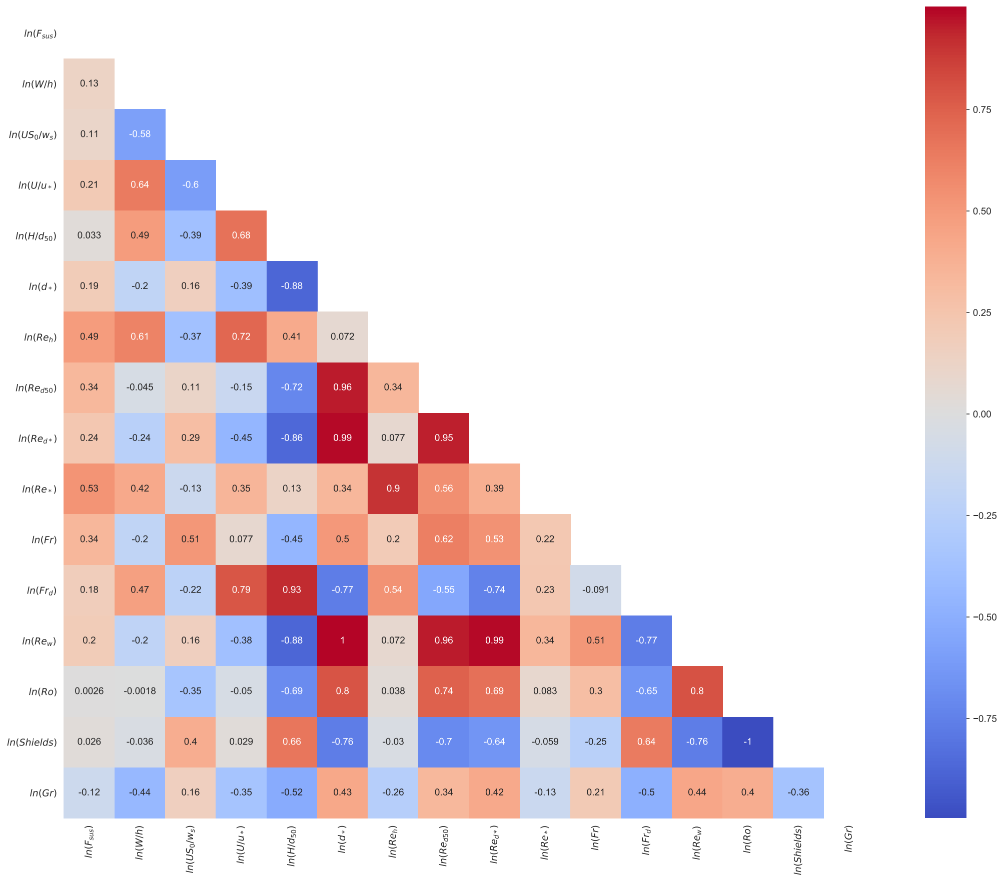

Figure 9. Correlation heat map for all dimensionless variables

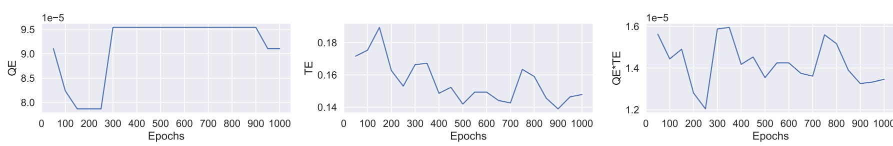

Figure 10. QE and TE epochs for the seven dimensionless variables [F_{sus}, W/h, d_*, Re_h, Fr, Fr_d, and Re_w]

The iterative GMM procedure is illustrated in Figure 11. The figure shows the minimum scores for each cluster. The minimal AIC+BIC value was 5. However, $K = 4$ was selected because the BIC increased when $K > 4$.

To analyze the SOM-GMM results, two cluster plots were drawn. Figure 13 shows a pair of scatter plots, and Figure 12 shows the corresponding SOM component planes.

Based on the frequency of the dimensionless variables, it is evident that Re_h and Fr_d are sufficiently informative to explain F_{sus} through the following inferences. First, all of the dimensionless numbers, excluding the slope-related numbers U_* and S_0 with high uncertainties, can be approximated by combining Re_h and Fr_d. For example, $Re_h Fr_d = f(h/\sqrt{d_{50}})$, such that h/d_{50} can be expressed in a scaled manner. As shown in Table 2, Fr_d is considered as the main input variable, especially in recent studies (Tayfur et al., 2013; Okcu et al., 2016). With respect to physical inference, these two variables are related to suspended and bed loads. The Reynolds number is known as the turbulence cri-

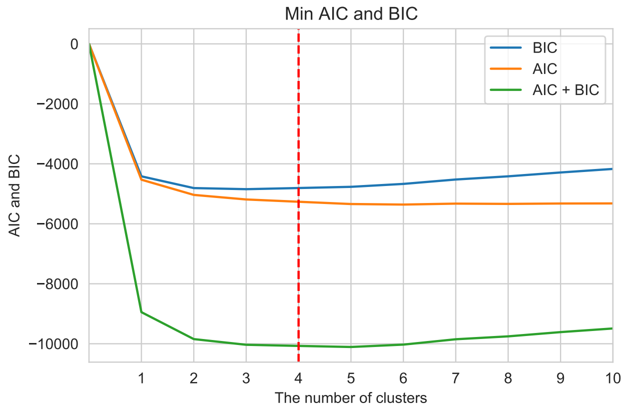

Figure 11. Minimum AIC+BIC values for each cluster number for the seven dimensionless variables [F_{sus}, W/h, d_*, Re_h, Fr, Fr_d, and Re_w]

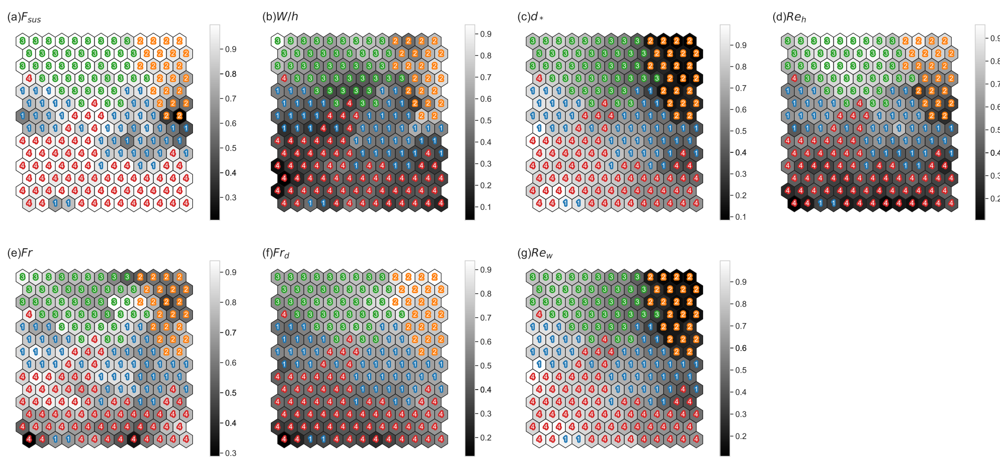

Figure 12. Component planes of the trained SOM grid: (a) F_{sus}; (b) W/h; (c) d_*; (d) Re_h; (e) Fr; (f) Fr_d; (g) Re_w

terion. Thus, Re_h may contribute to increasing the turbulent diffusion, causing particles to remain in suspension. The imbalance of the drag force on a single particle and the friction between the particle and bed materials initiate incipient motions (e.g., sliding, saltating, etc.). Fr_d is identical to the drag-bed friction balance, which can be expressed using Equation 42.

$$\frac{\text{Drag force}}{\text{Friction force}} = \frac{C_d \pi r_p^2 u^2}{\lambda_f N} = \frac{C_d \pi r_p^2 u^2}{\lambda_f g(G_s-1)\pi \frac{4}{3} r_p^3} = f(\frac{u^2}{g(G_s-1)r_p}) = f(Fr_d^2), \tag{42}$$

where C_d denotes the drag coefficient, r_p denotes the particle radius, u_p denotes the effective velocity of the particle, λ_f denotes the friction coefficient on the bed, and N is the normal force.

The relevance of F_{sus} has been emphasized in various studies. Hager (2018) highlighted Fr_d, also known as a densimetric Froude number, as the main parameter along with d_{50}/h in the bed load transport mechanism. In the sewer deposition problem, Fr_d has been considered the target parameter in many studies, and Fr_d can be a function of d_{50}/R_h (Safari & Mehr, 2018). In another aspect, with respect to coastal or ocean en-

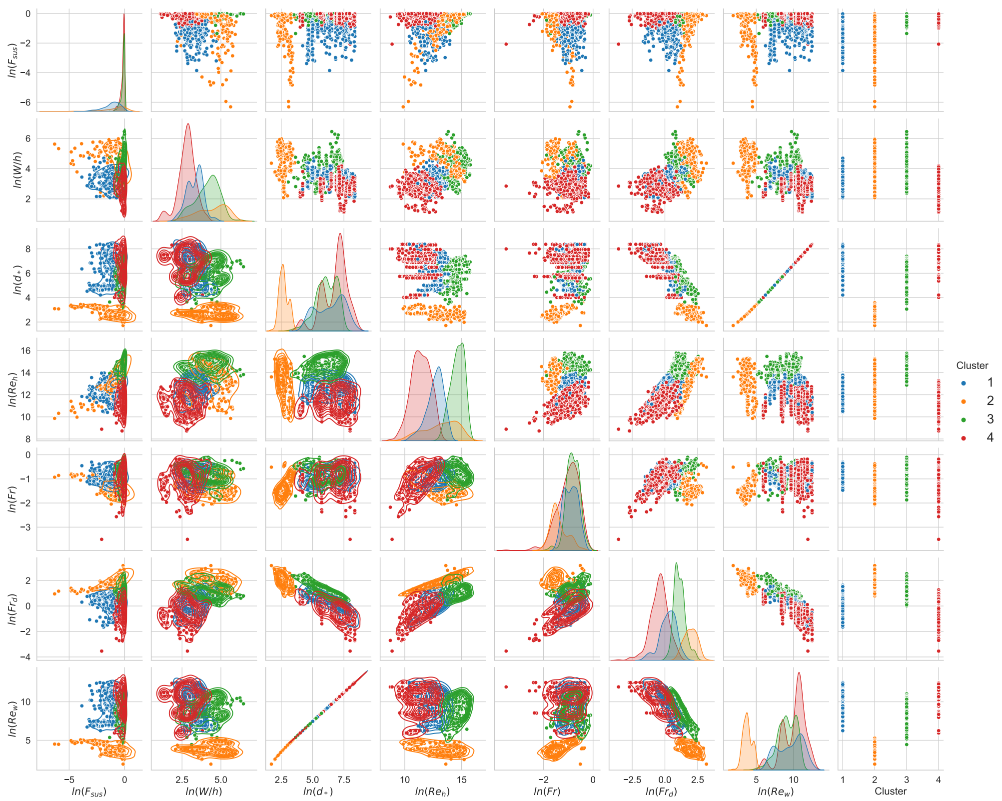

Figure 13. Pair scatter plots for the seven dimensionless variables [F_{sus}, W/h, d_*, Re_h, Fr, Fr_d, and Re_w]

vironments, similar interpretations have been conveyed by Fischer et al. (2002), regarding the denominator of Equation (42) as a representation of the buoyancy force.

In the high Re_h region, F_{sus} converges to 1. In the case of sufficiently strong turbulence dispersion forces, the bed loads in an unmeasured area of suspended samplers are suspended and dispersed to the measurable area, corresponding to the suspended sediment region. Consequently, the intense suspension allows suspended sediment loads to be approximated to the total sediment loads (as shown in Figure 15).

As observed from the structures of MGGP3 and Operon3, Fr, which is always accompanied by Re_h, plays a role in scaling h. Furthermore, $Fr^2 = U^2/(gh)$ is the ratio of the flow energy head to the suspended sediment region. For $h = h_s + h_b$, where h_s and h_b represent the suspended sediment and bed load regions, respectively, h_b is constant owing to the sampler size, and thus, a variation in h indicates a variation in h_s. If the flow velocity is fixed, a decrease in Fr implies an increase in h_s, which in turn increases Q_s. In terms of fixing the water depth h, laboratory experiments demonstrated that the suspended load contribution increases for larger Fr in dune migration dominated by bed loads (Naqshband et al., 2014). In Figures 15 and 12, the cover range of a low Fr decreases in the order of red, blue, and orange clusters for $12 < ln(Re_h) < 14$. For the same Re_h value, F_{sus} increases in the same order, thus supporting the above inference.

In both MGGP5 and Operon5 formulations, W/h accompanies d_*. Stewart (1983) reported that the fluvial channel, predominantly composed of suspended sediment, possessed features, such as silt/clay and steep bench/point bar, owing to a low W/h. In morphological transitions, streams with low W/h are likely to be eroded, and excessive deposition occurs in streams with high W/h (D. L. Rosgen, 1994; D. Rosgen, 2019). Another report (Edwards et al., 1999) describes the influence of W/h on F_{sus} and its temporal change. For fine bed materials, W/h can be reciprocal to C_w. According to a previous study (Xu, 2002), W/h can have a positive relation with C_w for low C_w, with the assumption that for a coarser grain, the flow is prone to be related to bed load. The low W/h coverage is smaller in the order of red, blue, orange, and green clusters for $ln(Re_h) < 12.5$. F_{sus} decreases in the order of the red, blue, and orange clusters. However, F_{sus} for the green cluster is the largest, despite the high W/h and d_*. As shown in the upper two rows of Figures 12 (b) and 12(c), the green cluster is characterized by a high Re_h. For large total loads, the Q_t fraction becomes dominant, as depicted by the linearly increasing lower bound in the 1×4 plot in Figure 13. This suspended sediment-dominant flow of the green cluster was due to the excessively large Re_h. The nonlinear relation between W/h and d_* in MGGP5 and Operon5 is valid for the calibration of the regime shift. The same interpretation can be applied to Re_w because its correlation to d_* is 1 and curved for low Re_w (the orange cluster).

6.2 Sensitivity Analysis

This section presents the sensitivity of the models developed in this study obtained by changing the input variables. The sensitivity analysis was conducted on Operon3 and SVR5, the best explicit and implicit models, respectively. In addition, a sensitivity analysis was conducted on SVR3 to inspect the effect of a nonlinear complexity increase.

Figure 14 presents the one-at-a-time (OAT) sensitivity analysis results. The upper plots are spyder plots indicating the change in F_{sus} owing to a 50% variation in the input variables. The sensitivity index (SI) defined by Equation 43 is computed for quantitative comparison.

$$SI = \frac{max(F_{sus}) - min(F_{sus})}{max(F_{sus})} \tag{43}$$

For perceptibility, three-dimensional surface plots were drawn using the two influential variables Fr_d and Re_h.

The most sensitive variable in the case of Operon3 is Re_h (SI = 0.4024) in a positive relationship. Fr_d is reciprocal to F_{sus} and only half as influential as Re_h. Fr is the most insensitive variable with an SI value of 0.149 and an exponential-like increment.

The effect of Re_h is prominent (SI = 0.5306). F_{sus} diminishes after a change of 120%. The increasing and decreasing behavior was observed for both Fr_d and Fr, but the fluctuation in Fr was exceptional. The fluctuation observed in Operon3 indicates a nonlinear relationship between the three variables.

In SVR5, the curves of Re_h and W/h resemble those in SVR3. The SI associated with W/h was the largest at 0.217. However, it was twice smaller than the maximum SI values obtained in the spyder plots of Operon3 and SVR3. This indicates the tuning effect of the two additional variables. d_* and Re_w demonstrated similar trends when increasing. For a negative change in d_*, F_{sus} drastically decreased with the local maximum point. Re_w, which represents the falling velocity, was negatively related to F_{sus}.

The proportionality of Re_h is clearly illustrated in the bottom row of Figure 14. For Operon3 and SVR3, the sensitivity of Fr_d is as high as Re_h is small. The surfaces of SVR3 and SVR5 have local maximum points. However, F_{sus} increases corresponding to Fr_d, as shown in Figure 14(f). This growth may be because SVR5 expresses the grain-size effect using not only Fr_d but also d_* and Re_w.

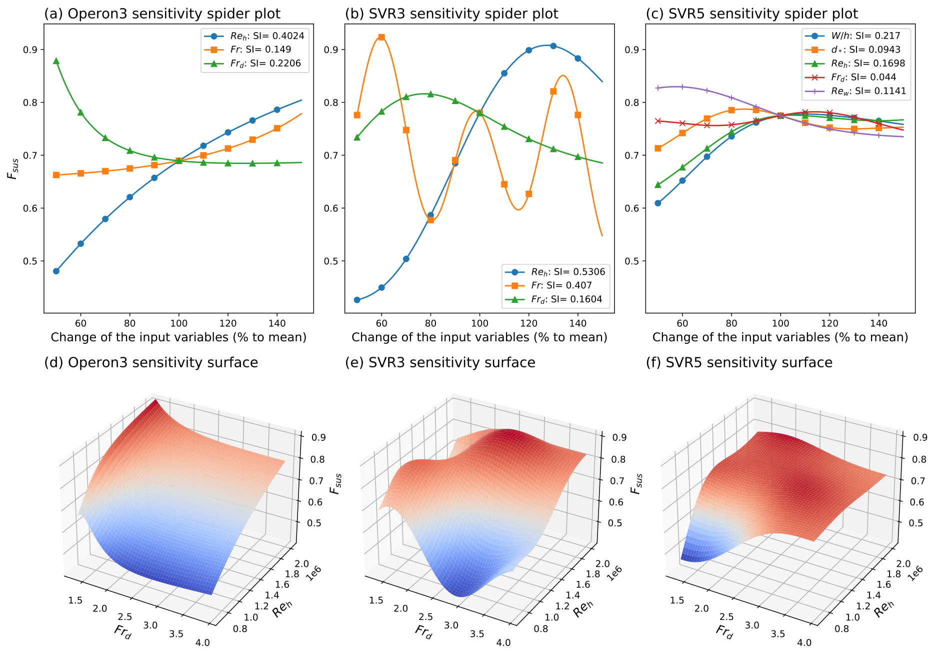

Figure 14. Spyder and three-dimensional surface plots for the three proposed algebraic equations: (a,d) tanh-type; (b,e) MGGP1; (c,f) MGGP2.

6.3 Q_t Estimation Using F_{sus}

Overall, the analysis showed that SVR5 was the best model for estimating accuracy. In practical use, Operon3 shows promise considering its explicit expression. However, the underestimation of PBIAS amplifies Q_t in Operon3. By contrast, SVR5 is likely to underrate Q_t. Based on these characteristics, SVR5 is considered suitable for users who want to determine F_{sus} correctly. Operon3 can be appropriately used for conservative river channel designs.

The practical use of F_{sus} involves the estimation of the total load Q_t using the following relationship:

$$Q_t = Q_s + Q_b = \frac{Q_s}{F_{sus}} \tag{44}$$

Figure 15 shows the relationships between F_{sus}, Q_t, Q_s, and Q_b. Figure 15(b) shows that Q_s is distributed along the 1:1 line. In the physical sense, Q_s should be the lower limit of Q_t. For a highly tractive flow, water sweeps the bed material, resulting in rapid bed load transport. If the flow is sufficiently rapid to convey bed materials, there is also a high possibility of suspended sediment-governed flows that develop suspension. Thus, Q_s can be approximated as Q_t even though a large amount of Q_b is transported. However, Q_b contributes more to a low Q_s, as shown in the relationship between F_{sus} and Q_s.

Because Q_s dominates over Q_t, R^2 is equal to 0.999, where the R^2 value of Q_b is -0.027. However, estimating F_{sus} using only Q_s is not recommended because the R^2 evaluation yields a value of -8.753×10^6. Despite the high R^2, estimating Q_t using F_{sus} is advantageous over using only Q_s in a conservative design because an estimation using F_{sus} always yields $Q_t > Q_s$ with R^2 over 0.999.

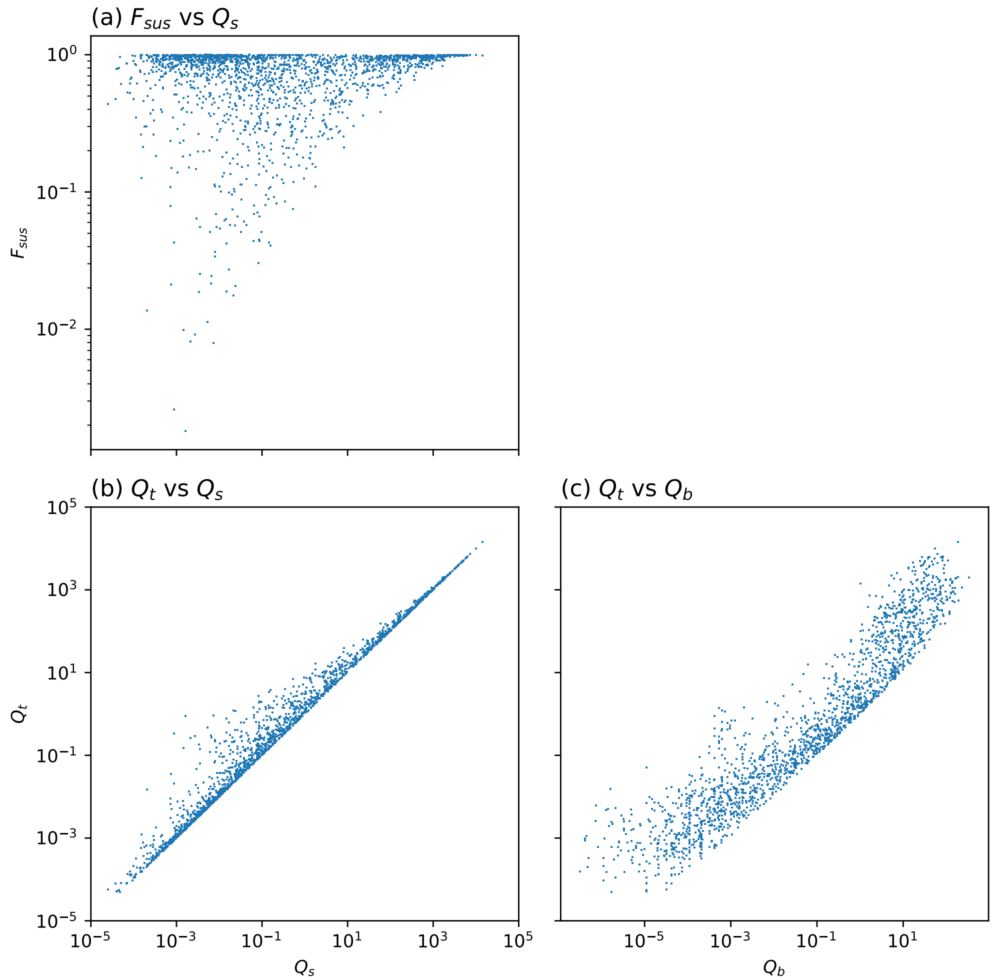

Figure 15. Scatter plots for F_{sus}, Q_t, Q_s, and Q_b

MEP interprets that the nonlinear relationship between the Rouse number Ro and d_{50} governs F_{sus}. The Einstein integral contains the velocity profile information from the turbulent velocity profile, causing the ratio of suspended load to total load to vary with d_s, h, and Ro (C.-Y. Yang & Julien, 2019). u_* in Ro alternatively depends on g, h, and S_0. An issue arises when our equations do not contain u_* and d_{ss}, which are key factors for Ro. In contrast, Lara (1966) proved that Ro could be estimated using $Ro = Aw_{ss}^B$. We believe that Ro can be implicitly applied as a nonlinear expression of the explicit equations obtained in this study.

Moreover, excluding u_* is beneficial for minimizing uncertainty. In other words, the strict measurement of the slopes for u_* is challenging because natural streams have various bedforms and platforms.

Essentially, MEPs assume sand-bed streams. In this context, Shah-Fairbank et al. (2011) observed that applying different schemes for Ro regimes was favorable because of the applicability of MEP. The suggested empirical models are widely applicable using a previously published dataset (Williams & Rosgen, 1989), which covers bed material sizes ranging from sand (0.28 mm) to cobbles (216 mm).

Recently, river-monitoring techniques have been developed. The empirical models designed in this study can be implemented in recently developed flow-suspended sediment-monitoring techniques to estimate Q_t because the required input variables can be obtained by these techniques. For example, at the river scale, drone-based remote-sensing techniques have been applied to suspended sediment concentrations (Kwon, Shin, et al., 2022; Kwon, Seo, et al., 2022), bathymetry, and flows (Legleiter & Harrison, 2019; Legleiter & Kinzel, 2021; Eltner et al., 2020). ADCPs can be utilized for the simultaneous measurement of flow and suspended sediment (Son et al., 2021; Noh et al., 2022). For bed grain-size estimation, one method is to use image-processing software packages, such as pyDGS (Buscombe, 2013) and Basegrain (Detert & Weitbrecht, 2012); however, sieving is the only reliable method that can be used for sand or finer grains (Harvey et al., 2022). If sieving is the only option, it is advantageous to create a dictionary of the mean size of bed material on the probable areas before applying the above methods. If the aforementioned monitoring technologies can be combined and applied appropriately, safety and cost minimization can be achieved.

7 Concluding Remarks

This study proposes estimation models based on machine learning for the estimation F_{sus}, which is defined as the ratio of the suspended load to the total sediment load. Six models were developed using SVR, representing the black-box method and two state-of-the-art symbolic regression models, namely, MGGP and Operon. Prior to the formulation, the hydromorphic variables were non-dimensionalized. The two-stage clustering algorithm SOM-GMM was used to analyze the F_{sus} reaction by changing the dimensionless hydromorphic variables. In addition, an OAT sensitivity analysis was conducted.

The input variable selection and parameter tuning of the machine-learning methods were based on GRID-RFE-CV. From the feature elimination step, two distinguished parameter combinations were observed: 1)W/h, d_*, Re_h, Fr_d, and Re_w, and 2) Re_h, Fr, and Fr_d. For estimation accuracy, each machine-learning method was trained using two optimal variable combinations, producing six models. The performance criteria suggest that SVR5 outperforms all other models, and Operon3 is the most accurate explicit model. In the analysis of the empirical equations and clustering results, Re_h and Fr_d frequently appear to be influential.

The models proposed in this study require the basic hydraulic features U, W, h, and d_{50}, excluding the u_* related variables, that are generally adopted for sediment load estimation. Subsequently, Q_s and the aforementioned basic hydraulic features are necessary to estimate Q_t. For application to rivers with different characteristics from those of US streams, it is recommended to train the models using a specific environment because the dataset exploited in this study consists of US streams.

Data Availability Statement

Datasets used for derivation of the F_{sus} estimation models were obtained from the referenced article: Williams and Rosgen (1989). The data of the derived models and example scripts in Python language are available at the GitHub repository: `https://github.com/hyoddubi1/Fsus-sediment-fraction-models`.

Acknowledgments

This research was partially supported by the Korea Technology & Information Promotion Agency for SMEs grant funded by Ministry of SMEs and Startups (Grant S3251997), and the Korea Agency for Infrastructure Technology Advancement(KAIA) grant funded by the Ministry of Land, Infrastructure and Transport (Grant 22DPIW-C153746-04).

We also appreciate Institute of Engineering Research at Seoul National University, Seoul, Korea.

References

Ackers, P., & White, W. R. (1973). Sediment transport: new approach and analysis. *Journal of the Hydraulics Division*, *99*(11), 2041–2060.

Agrawal, Y. C., & Pottsmith, H. C. (2000). Instruments for particle size and settling velocity observations in sediment transport. *Marine Geology*, *168*(1-4), 89–114.

Akaike, H. (1974). A new look at the statistical model identification. *IEEE transactions on automatic control*, *19*(6), 716–723.

Alvarez-Guerra, M., González-Piñuela, C., Andrés, A., Galán, B., & Viguri, J. R. (2008). Assessment of self-organizing map artificial neural networks for the classification of sediment quality. *Environment International*, *34*(6), 782–790.

Bagnold, R. A. (1966). *An approach to the sediment transport problem from general physics*. US government printing office.

Bezdek, J. C., Ehrlich, R., & Full, W. (1984). Fcm: The fuzzy c-means clustering algorithm. *Computers & geosciences*, *10*(2-3), 191–203.

Bishop, C. M. (2006). Pattern recognition. *Machine learning*, *128*(9).

Burlacu, B., Kronberger, G., & Kommenda, M. (2020). Operon c++ an efficient genetic programming framework for symbolic regression. In *Proceedings of the 2020 genetic and evolutionary computation conference companion* (pp. 1562–1570).

Buscombe, D. (2013). Transferable wavelet method for grain-size distribution from images of sediment surfaces and thin sections, and other natural granular patterns. *Sedimentology*, *60*(7), 1709–1732.

Civan, F. (2007). Critical modification to the vogel- tammann- fulcher equation for temperature effect on the density of water. *Industrial & engineering chemistry research*, *46*(17), 5810–5814.

Colby, B. R., & Hembree, C. H. (1954). Computations of total sediment discharge, niobrara river near cody, nebraska. *Science*, *119*(3097), 657–658.

DDBST GmbH. (n.d.). *Liquid dynamic viscosity.* `http://ddbonline.ddbst.de/VogelCalculation/VogelCalculationCGI.exe?component=Water`. Oldenburg, Germany. (Accessed: 2022-11-09)

Dempster, A. P., Laird, N. M., & Rubin, D. B. (1977). Maximum likelihood from incomplete data via the em algorithm. *Journal of the Royal Statistical Society: Series B (Methodological)*, *39*(1), 1–22.

Detert, M., & Weitbrecht, V. (2012). Automatic object detection to analyze the geometry of gravel grains–a free stand-alone tool. In *River flow* (pp. 595–600).

Drucker, H., Burges, C. J., Kaufman, L., Smola, A., & Vapnik, V. (1996). Support vector regression machines. *Advances in neural information processing systems*, *9*.

Edwards, T. K., Glysson, G. D., Guy, H. P., & Norman, V. W. (1999). *Field methods for measurement of fluvial sediment*. US Geological Survey Denver, CO.

Eltner, A., Sardemann, H., & Grundmann, J. (2020). Flow velocity and discharge measurement in rivers using terrestrial and unmanned-aerial-vehicle imagery. *Hydrology and Earth System Sciences*, *24*(3), 1429–1445.

Engelund, F., & Hansen, E. (1967). A monograph on sediment transport in alluvial streams. *Technical University of Denmark 0stervoldgade 10, Copenhagen K.*.

Fischer, P. F., Leaf, G. K., & Restrepo, J. M. (2002). Forces on particles in oscillatory boundary layers. *Journal of Fluid Mechanics*, *468*, 327–347.

Gellis, A. C. (2013). Factors influencing storm-generated suspended-sediment concentrations and loads in four basins of contrasting land use, humid-tropical puerto rico. *Catena*, *104*, 39–57.

Guyon, I., Weston, J., Barnhill, S., & Vapnik, V. (2002). Gene selection for cancer classification using support vector machines. *Machine learning*, *46*(1), 389–422.

Hager, W. H. (2018). Bed-load transport: advances up to 1945 and outlook into the future. *Journal of Hydraulic Research*, *56*(5), 596–607.

Harvey, E. L., Hales, T. C., Hobley, D. E., Liu, J., & Fan, X. (2022). Measuring the grain-size distributions of mass movement deposits. *Earth Surface Processes and Landforms*.

Heil, J., Häring, V., Marschner, B., & Stumpe, B. (2019). Advantages of fuzzy k-means over k-means clustering in the classification of diffuse reflectance soil spectra: A case study with west african soils. *Geoderma*, *337*, 11–21.

Holmquist-johnson, C. L. (2006). *Bureau of reclamation automated modified einstein procedure (boramep) program for computing total sediment load.*

Jain, A. K. (2010). Data clustering: 50 years beyond k-means. *Pattern recognition letters*, *31*(8), 651–666.

Julien, P. Y. (2010). *Erosion and sedimentation.* Cambridge university press.

Karim, F. (1998). Bed material discharge prediction for nonuniform bed sediments. *Journal of Hydraulic Engineering*, *124*(6), 597–604.

Kim, K.-H., Yun, S.-T., Yu, S., Choi, B.-Y., Kim, M.-J., & Lee, K.-J. (2020). Geochemical pattern recognitions of deep thermal groundwater in south korea using self-organizing map: Identified pathways of geochemical reaction and mixing. *Journal of Hydrology*, *589*, 125202.

Kiviluoto, K. (1996). Topology preservation in self-organizing maps. In *Proceedings of international conference on neural networks (icnn'96)* (Vol. 1, pp. 294–299).

Kohonen, T. (1990). The self-organizing map. *Proceedings of the IEEE*, *78*(9), 1464–1480.

Kohonen, T. (2012). *Self-organizing maps* (Vol. 30). Springer Science & Business Media.

Kohonen, T. (2013). Essentials of the self-organizing map. *Neural networks*, *37*, 52–65.

Koza, J. R. (1992). *Genetic programming: on the programming of computers by means of natural selection* (Vol. 1). MIT press.

Kwon, S., Seo, I. W., Noh, H., & Kim, B. (2022). Hyperspectral retrievals of suspended sediment using cluster-based machine learning regression in shallow waters. *Science of The Total Environment*, *833*, 155168. Retrieved from `https://www.sciencedirect.com/science/article/pii/S0048969722022616` doi: https://doi.org/10.1016/j.scitotenv.2022.155168

Kwon, S., Shin, J., Seo, I. W., Noh, H., Jung, S. H., & You, H. (2022). Measurement of suspended sediment concentration in open channel flows based on hyperspectral imagery from uavs. *Advances in Water Resources*, *159*, 104076.

La Cava, W., Orzechowski, P., Burlacu, B., de França, F. O., Virgolin, M., Jin, Y., … Moore, J. H. (2021). Contemporary symbolic regression methods and their relative performance. *arXiv preprint arXiv:2107.14351*.

Lara, J. M. (1966). *Computation of "z's" for use in the modified einstein procedure.* Department of the Interior, Bureau of Reclamation, Office of Chief Engineer, Denver.

Legleiter, C. J., & Harrison, L. R. (2019). Remote sensing of river bathymetry: Evaluating a range of sensors, platforms, and algorithms on the upper sacramento river, california, usa. *Water Resources Research*, *55*(3), 2142–2169.

Legleiter, C. J., & Kinzel, P. J. (2021). Improving remotely sensed river bathymetry by image-averaging. *Water Resources Research*, *57*(3), e2020WR028795.

Li, T., Sun, G., Yang, C., Liang, K., Ma, S., & Huang, L. (2018). Using self-organizing map for coastal water quality classification: Towards a better understanding of patterns and processes. *Science of the Total Environment*, *628*, 1446–1459.

Ma, X., Zhang, Y., & Wang, Y. (2015). Performance evaluation of kernel functions based on grid search for support vector regression. In *2015 ieee 7th international conference on cybernetics and intelligent systems (cis) and ieee conference on robotics, automation and mechatronics (ram)* (pp. 283–288).

Molinas, A., & Wu, B. (2001). Transport of sediment in large sand-bed rivers. *Journal of Hydraulic Research*, *39*(2), 135-146. Retrieved from `https://doi.org/10.1080/00221680109499814` doi: 10.1080/00221680109499814

Naqshband, S., Ribberink, J. S., Hurther, D., & Hulscher, S. J. (2014). Bed load and suspended load contributions to migrating sand dunes in equilibrium. *Journal of Geophysical Research: Earth Surface*, *119*(5), 1043–1063.

Noh, H., Park, Y. S., & Lee, M. (2021). Regional classification of total suspended matter in coastal areas of south korea. *Estuarine, Coastal and Shelf Science*, *254*, 107339.

Noh, H., Son, G., Kim, D., & Park, Y. S. (2022). Clustering of sediment characteristics in south korean rivers and its expanded application strategy to h-adcp based suspended sediment concentration monitoring technique. *Journal of Korea Water Resources Association*, *55*(1), 43–57.

Okcu, D., Pektas, A. O., & Uyumaz, A. (2016). Creating a non-linear total sediment load formula using polynomial best subset regression model. *Journal of Hydrology*, *539*, 662–673.

Ouillon, S. (2018). *Why and how do we study sediment transport? focus on coastal zones and ongoing methods* (Vol. 10) (No. 4). MDPI.

Oyelade, J., Isewon, I., Oladipupo, F., Aromolaran, O., Uwoghiren, E., Ameh, F., . . . Adebiyi, E. (2016). Clustering algorithms: their application to gene expression data. *Bioinformatics and Biology insights*, *10*, BBI–S38316.

Rosgen, D. (2019). The rosgen stream classification system. *Encyclopedia of Water: Science, Technology, and Society*, 1–15.

Rosgen, D. L. (1994). A classification of natural rivers. *Catena*, *22*(3), 169–199.

Safari, M. J. S., & Mehr, A. D. (2018). Multigene genetic programming for sediment transport modeling in sewers for conditions of non-deposition with a bed deposit. *International Journal of Sediment Research*, *33*(3), 262–270.

Schwarz, G. (1978). Estimating the dimension of a model. *The annals of statistics*, 461–464.

Searson, D. P. (2015). Gptips 2: an open-source software platform for symbolic data mining. In *Handbook of genetic programming applications* (pp. 551–573). Springer.

Shah-Fairbank, S. C., & Julien, P. Y. (2015). Sediment load calculations from point measurements in sand-bed rivers. *International Journal of Sediment Research*, *30*(1), 1–12.

Shah-Fairbank, S. C., Julien, P. Y., & Baird, D. C. (2011). Total sediment load from semep using depth-integrated concentration measurements. *Journal of Hydraulic Engineering*, *137*(12), 1606–1614.

Shen, H., & Hung, C. (1972). An engineering approach to total bed-material load by regression analysis. In *Proc. of sedimentation symposium, berkeley, california.*

Smola, A. J., & Schölkopf, B. (2004). A tutorial on support vector regression. *Statistics and computing*, *14*(3), 199–222.

Son, G., Kim, D., Kwak, S., Kim, Y. D., & Lyu, S. (2021). Characterizing three-dimensional mixing process in river confluence using acoustical backscatter as surrogate of suspended sediment. *Journal of Korea Water Resources Association*, *54*(3), 167–179.

Stewart, D. (1983). Possible suspended-load channel deposits from the wealden group (lower cretaceous) of southern england. *Modern and ancient fluvial systems*, 369–384.

Sun, Y., Ding, S., Zhang, Z., & Jia, W. (2021). An improved grid search algorithm to optimize svr for prediction. *Soft Computing*, *25*(7), 5633–5644.

Tayfur, G., Karimi, Y., & Singh, V. P. (2013). Principle component analysis in conjuction with data driven methods for sediment load prediction. *Water resources management*, *27*(7), 2541–2554.

Turowski, J. M., Rickenmann, D., & Dadson, S. J. (2010). The partitioning of the total sediment load of a river into suspended load and bedload: a review of empirical data. *Sedimentology*, *57*(4), 1126–1146.

Van Rijn, L. C. (1993). *Principles of sediment transport in rivers, estuaries and coastal seas* (Vol. 1006). Aqua publications Amsterdam.

Vesanto, J., Himberg, J., Alhoniemi, E., & Parhankangas. (2000). *Som toolbox for matlab 5* (Tech. Rep. No. A57). Neural Networks Research Centre, Espoo, Finland: Helsinki University of Technology.

Vogel, H. (1921). Das temperaturabhängigkeitsgesetz der viskosität von flüssigkeitenn. *Phys. Z.*, *22*, 645–646.

Wagner, W., & Pruß, A. (2002). The iapws formulation 1995 for the thermodynamic properties of ordinary water substance for general and scientific use. *Journal of physical and chemical reference data*, *31*(2), 387–535.

Williams, G. P., & Rosgen, D. L. (1989). *Measured total sediment loads (suspended loads and bedloads) for 93 united states streams.* US Geological Survey Washington, DC.

Xu, J. (2002). Complex behaviour of natural sediment-carrying streamflows and the geomorphological implications. *Earth Surface Processes and Landforms: The Journal of the British Geomorphological Research Group*, *27*(7), 749–758.

Yang, C. T. (1979). Unit stream power equations for total load. *Journal of Hydrology*, *40*(1-2), 123–138.

Yang, C.-Y., & Julien, P. Y. (2019). The ratio of measured to total sediment discharge. *International Journal of Sediment Research*, *34*(3), 262–269.

Figure 1.

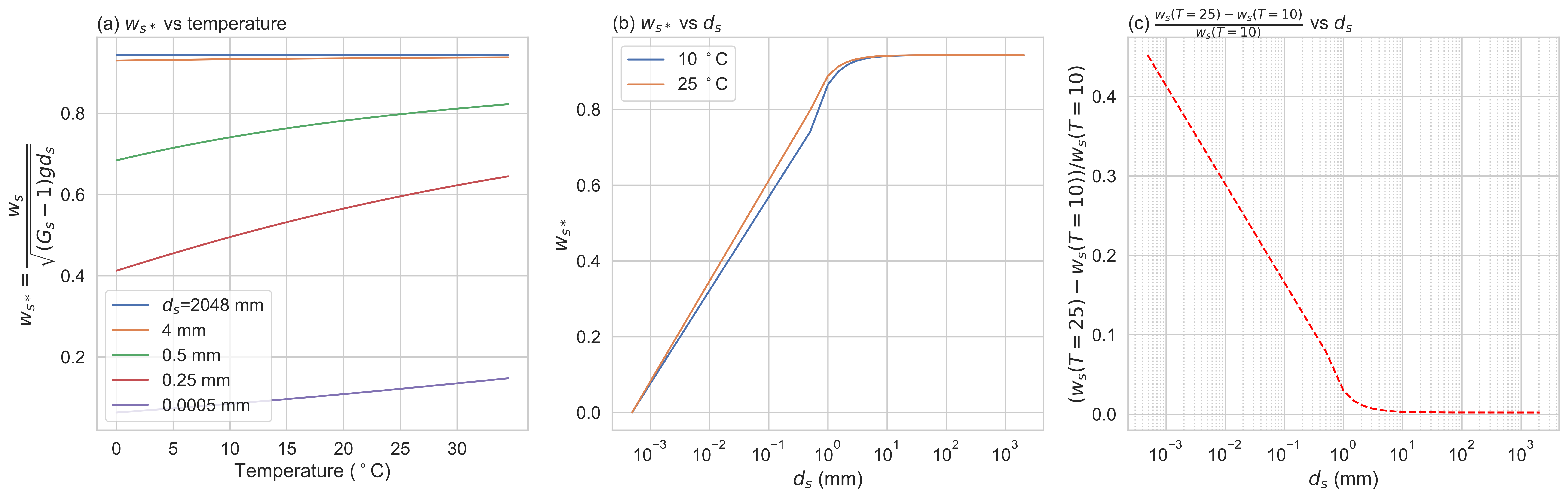

(a) w_{s*} vs temperature
$w_{s*} = \frac{w_s}{\sqrt{(G_s-1)gd_s}}$
0.2
0.4
0.6
0.8
0
5
10
15
20
25
30
Temperature ($^\circ$C)
d_s=2048 mm
4 mm
0.5 mm
0.25 mm
0.0005 mm
(b) w_{s*} vs d_s
w_{s*}
0.0
0.2
0.4
0.6
0.8
10^{-3}
10^{-2}
10^{-1}
10^{0}
10^{1}
10^{2}
10^{3}
d_s (mm)
10 $^\circ$C
25 $^\circ$C
(c) $\frac{w_s(T=25)-w_s(T=10)}{w_s(T=10)}$ vs d_s
$(w_s(T=25)-w_s(T=10))/w_s(T=10)$
0.0
0.1
0.2
0.3
0.4
10^{-3}
10^{-2}
10^{-1}
10^{0}
10^{1}
10^{2}
10^{3}
d_s (mm)

Figure 2.

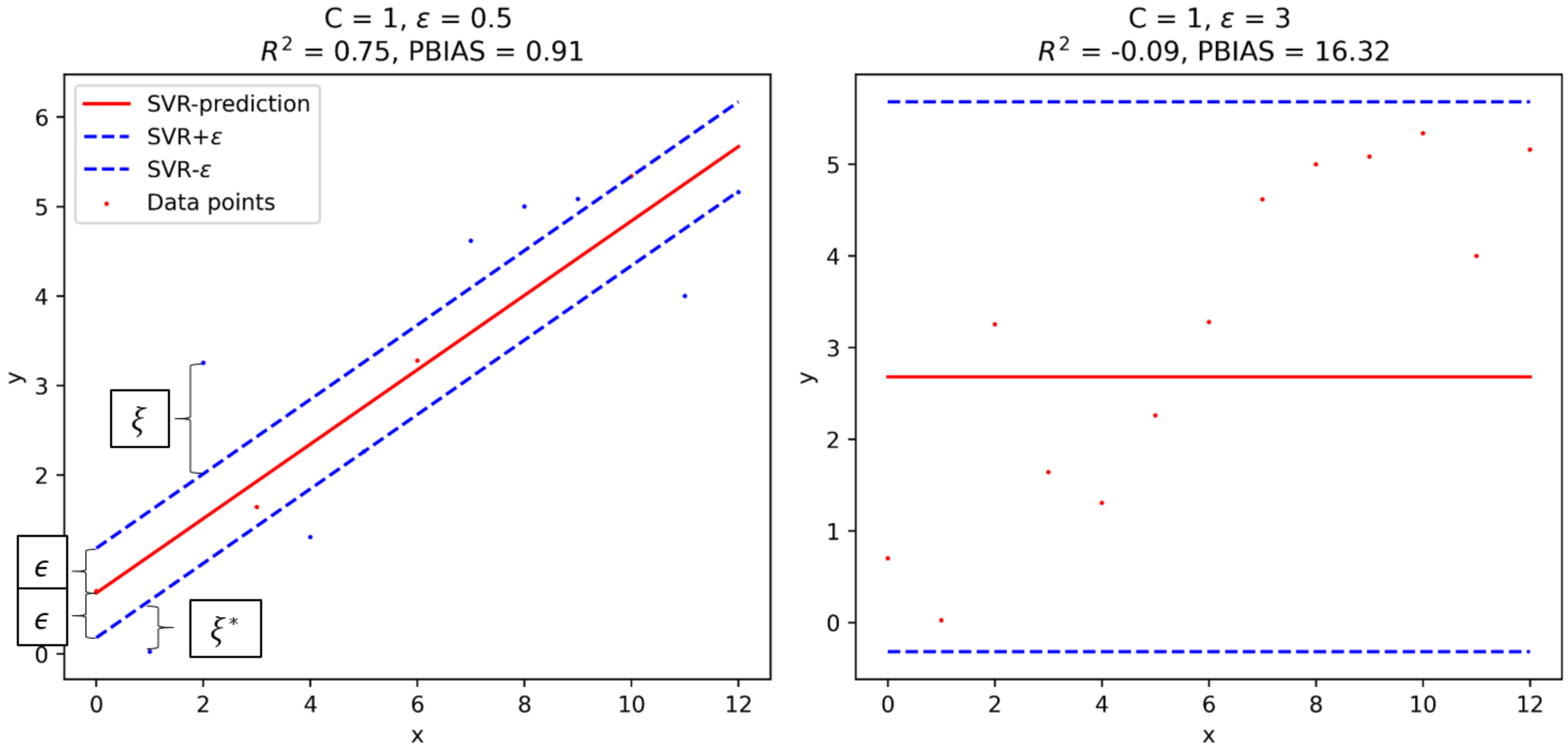
C = 1, ε = 0.5
R² = 0.75, PBIAS = 0.91
SVR-prediction
SVR+ε
SVR-ε
Data points
ξ
ϵ
ϵ
ξ*
y
x
C = 1, ε = 3
R² = -0.09, PBIAS = 16.32
y
x

Figure 3.

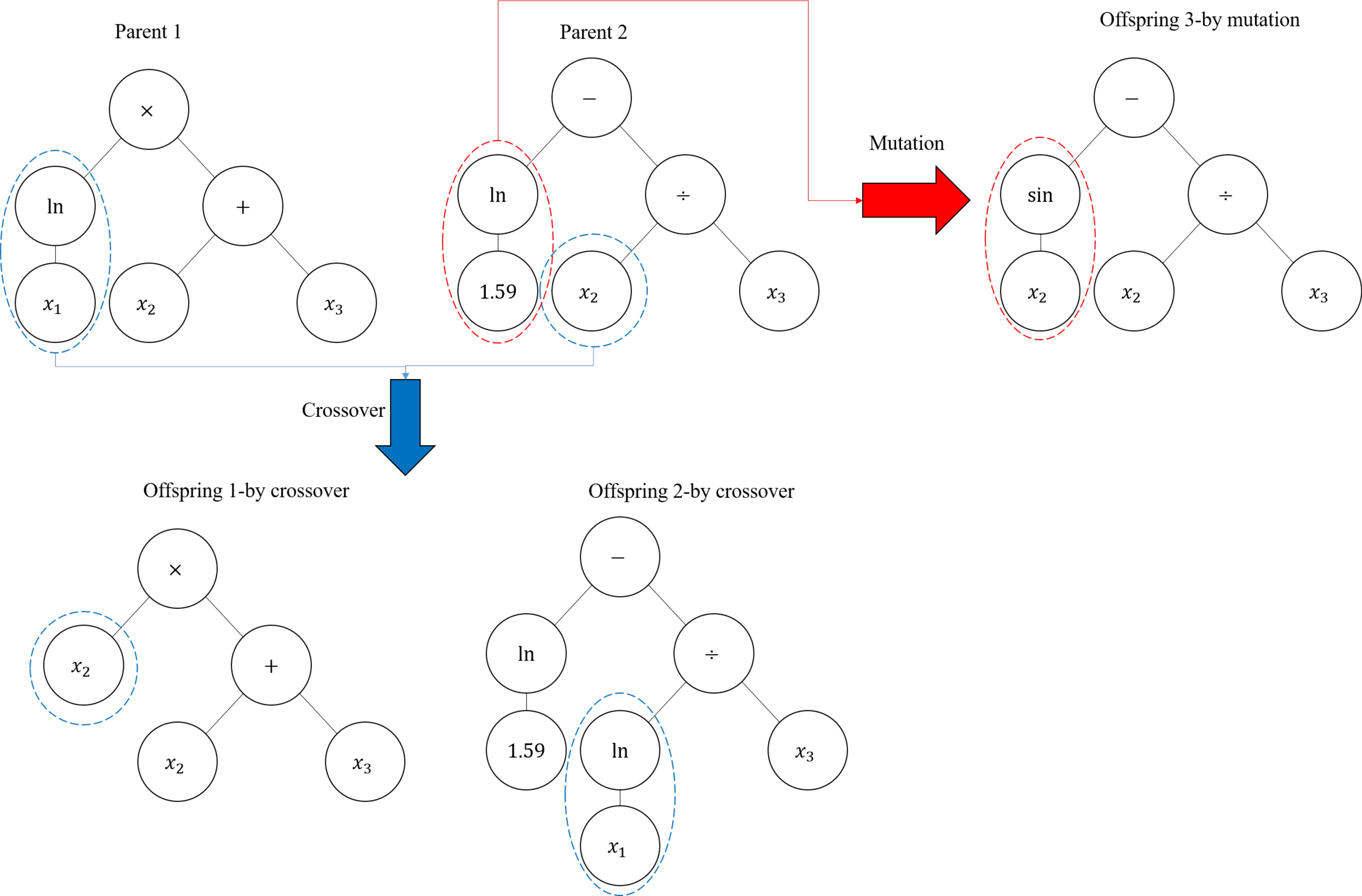
Parent 1
×
ln
+
x_1
x_2
x_3
Parent 2
−
ln
÷
1.59
x_2
x_3
Mutation
Offspring 3-by mutation
−
sin
÷
x_2
x_2
x_3
Crossover
Offspring 1-by crossover
×
x_2
+
x_2
x_3
Offspring 2-by crossover
−
ln
÷
1.59
ln
x_3
x_1

Figure 4.

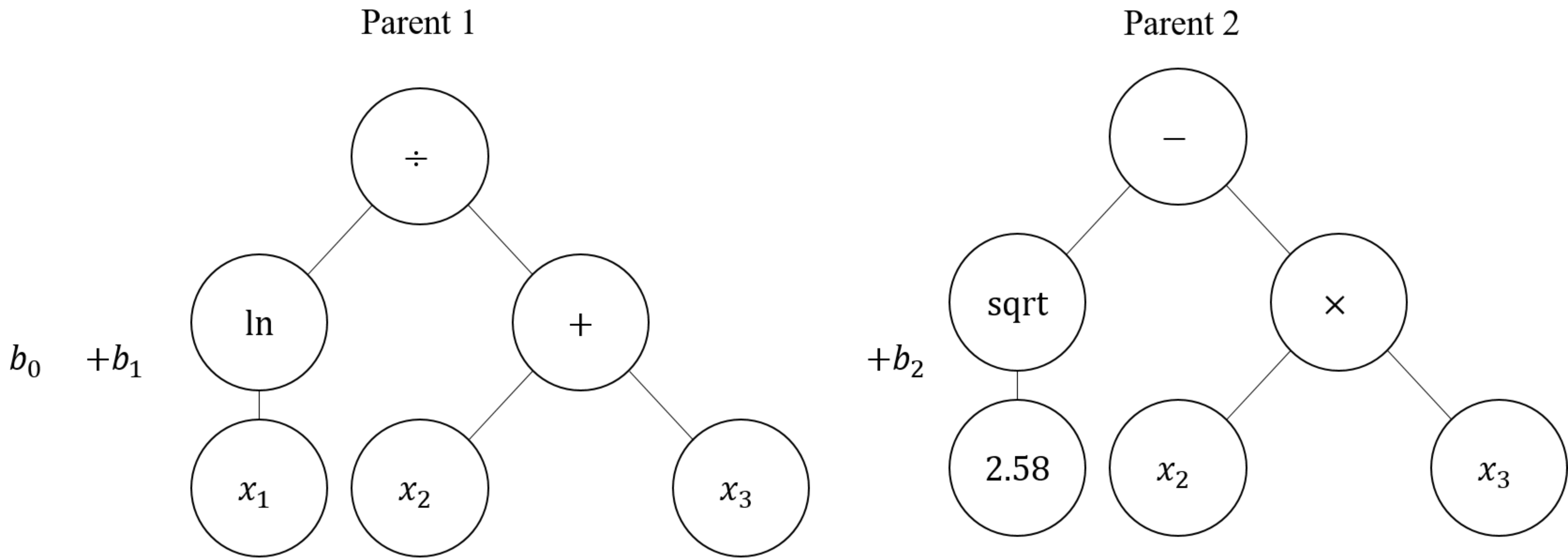

$$= b_0 + b_1\big(\ln(x_1) \div (x_2 + x_3)\big) + b_2\big(\sqrt{2.58} - x_2 \times x_3\big)$$

Figure 5.

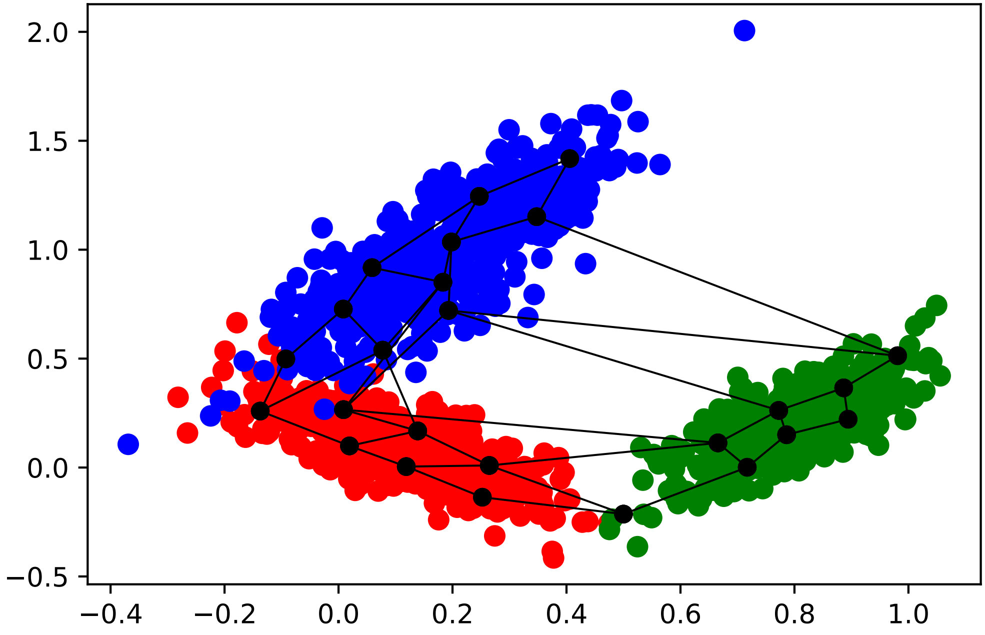
2.0
1.5
1.0
0.5
0.0
−0.5
−0.4
−0.2
0.0
0.2
0.4
0.6
0.8
1.0

Figure 6.

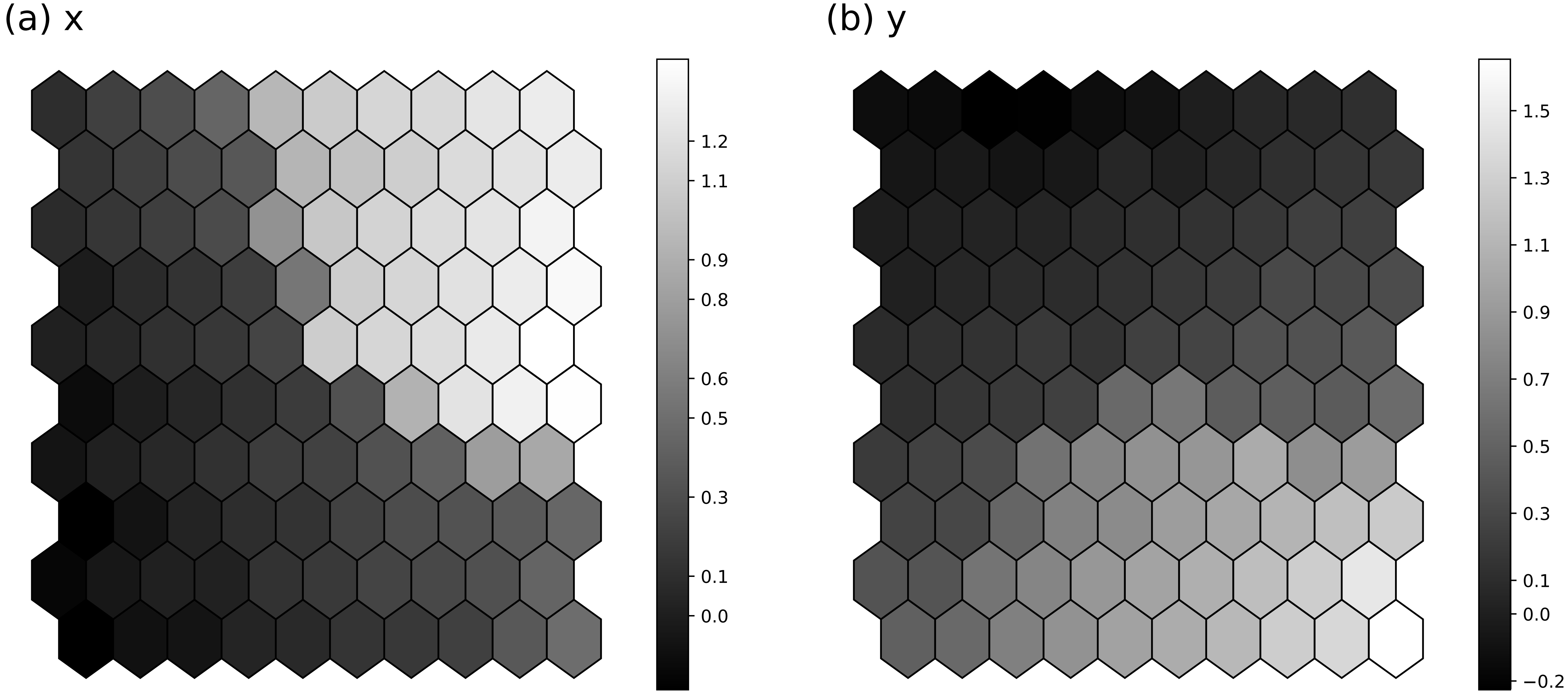
(a) x
1.2
1.1
0.9
0.8
0.6
0.5
0.3
0.1
0.0
(b) y
1.5
1.3
1.1
0.9
0.7
0.5
0.3
0.1
0.0
−0.2

Figure 7.

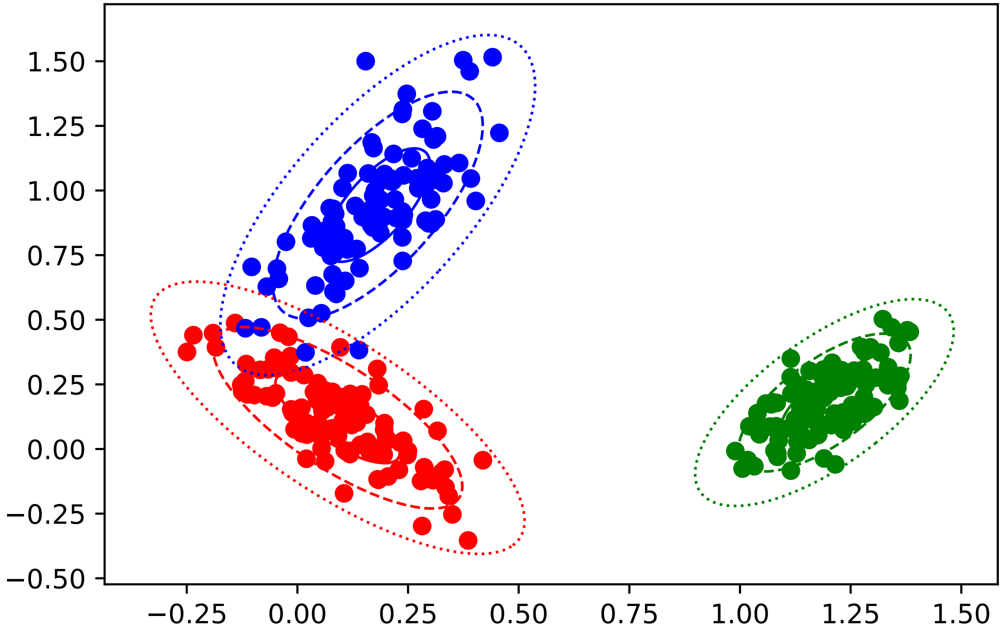
1.50
1.25
1.00
0.75
0.50
0.25
0.00
−0.25
−0.50
−0.25
0.00
0.25
0.50
0.75
1.00
1.25
1.50

Figure 8.

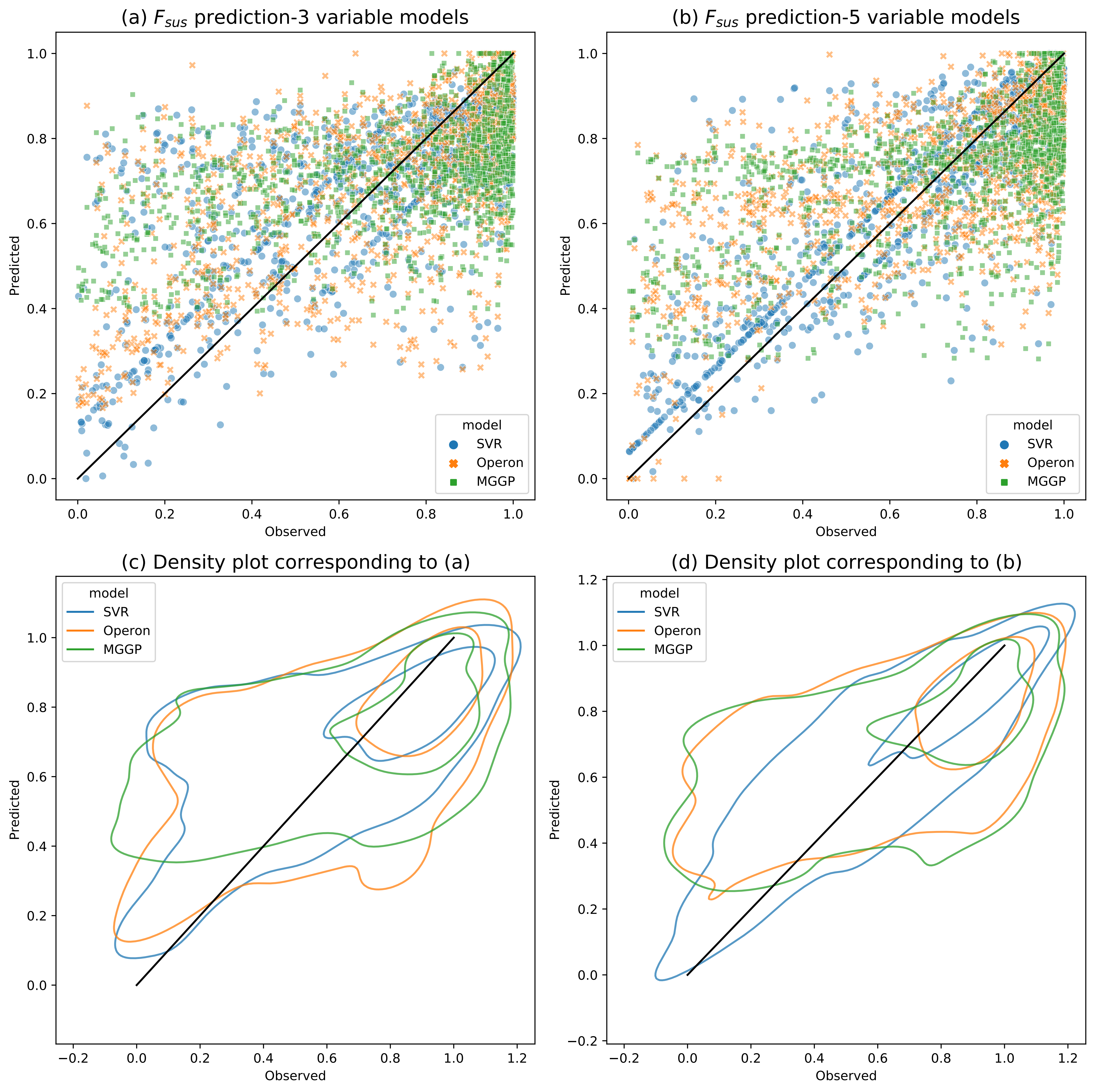

(a) F_{sus} prediction-3 variable models
(b) F_{sus} prediction-5 variable models
(c) Density plot corresponding to (a)
(d) Density plot corresponding to (b)
Predicted
Observed
model
SVR
Operon
MGGP

Figure 9.

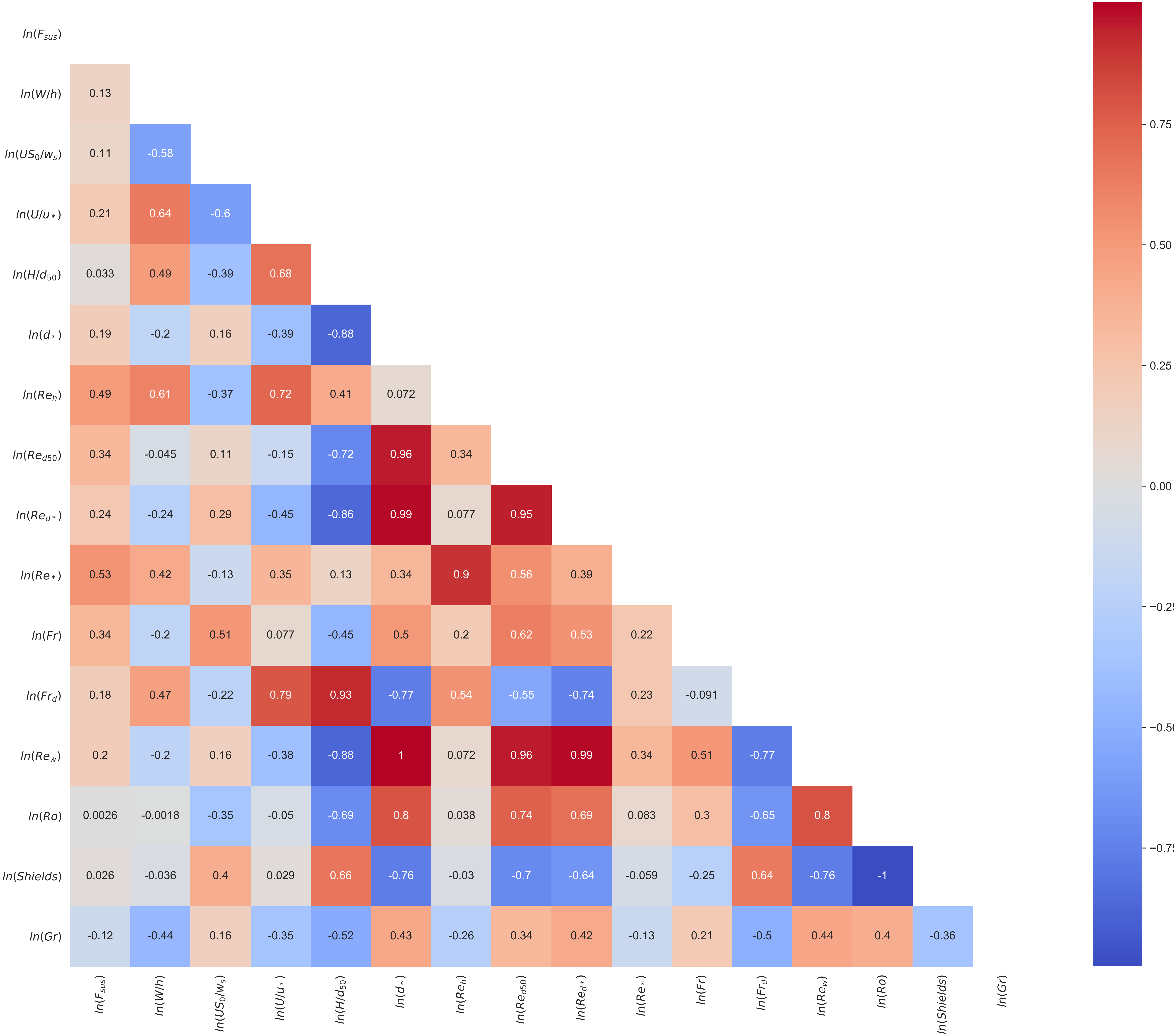

$ln(F_{sus})$
$ln(W/h)$ 0.13
$ln(US_0/w_s)$ 0.11 -0.58
$ln(U/u_*)$ 0.21 0.64 -0.6
$ln(H/d_{50})$ 0.033 0.49 -0.39 0.68
$ln(d_*)$ 0.19 -0.2 0.16 -0.39 -0.88
$ln(Re_h)$ 0.49 0.61 -0.37 0.72 0.41 0.072
$ln(Re_{d50})$ 0.34 -0.045 0.11 -0.15 -0.72 0.96 0.34
$ln(Re_{d*})$ 0.24 -0.24 0.29 -0.45 -0.86 0.99 0.077 0.95
$ln(Re_*)$ 0.53 0.42 -0.13 0.35 0.13 0.34 0.9 0.56 0.39
$ln(Fr)$ 0.34 -0.2 0.51 0.077 -0.45 0.5 0.2 0.62 0.53 0.22
$ln(Fr_d)$ 0.18 0.47 -0.22 0.79 0.93 -0.77 0.54 -0.55 -0.74 0.23 -0.091
$ln(Re_w)$ 0.2 -0.2 0.16 -0.38 -0.88 1 0.072 0.96 0.99 0.34 0.51 -0.77
$ln(Ro)$ 0.0026 -0.0018 -0.35 -0.05 -0.69 0.8 0.038 0.74 0.69 0.083 0.3 -0.65 0.8
$ln(Shields)$ 0.026 -0.036 0.4 0.029 0.66 -0.76 -0.03 -0.7 -0.64 -0.059 -0.25 0.64 -0.76 -1
$ln(Gr)$ -0.12 -0.44 0.16 -0.35 -0.52 0.43 -0.26 0.34 0.42 -0.13 0.21 -0.5 0.44 0.4 -0.36
$ln(F_{sus})$ $ln(W/h)$ $ln(US_0/w_s)$ $ln(U/u_*)$ $ln(H/d_{50})$ $ln(d_*)$ $ln(Re_h)$ $ln(Re_{d50})$ $ln(Re_{d*})$ $ln(Re_*)$ $ln(Fr)$ $ln(Fr_d)$ $ln(Re_w)$ $ln(Ro)$ $ln(Shields)$ $ln(Gr)$
0.75
0.50
0.25
0.00
−0.25
−0.50
−0.75

Figure 10.

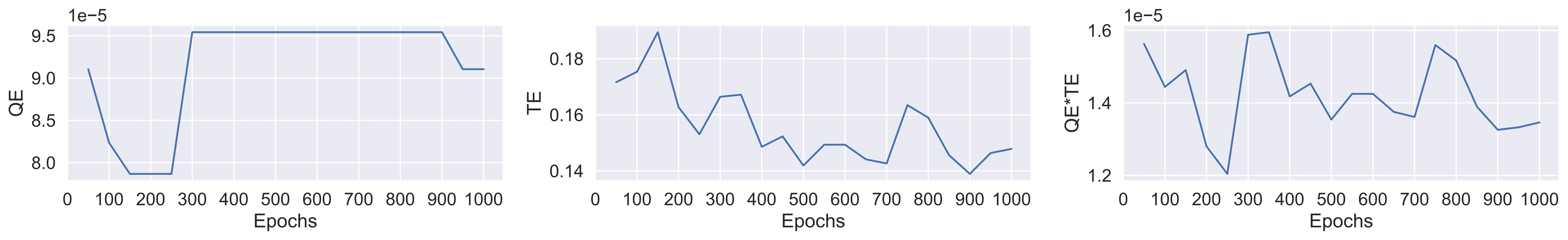
1e−5
QE
9.5
9.0
8.5
8.0
0
100
200
300
400
500
600
700
800
900
1000
Epochs
TE
0.18
0.16
0.14
Epochs
1e−5
QE*TE
1.6
1.4
1.2
Epochs

Figure 11.

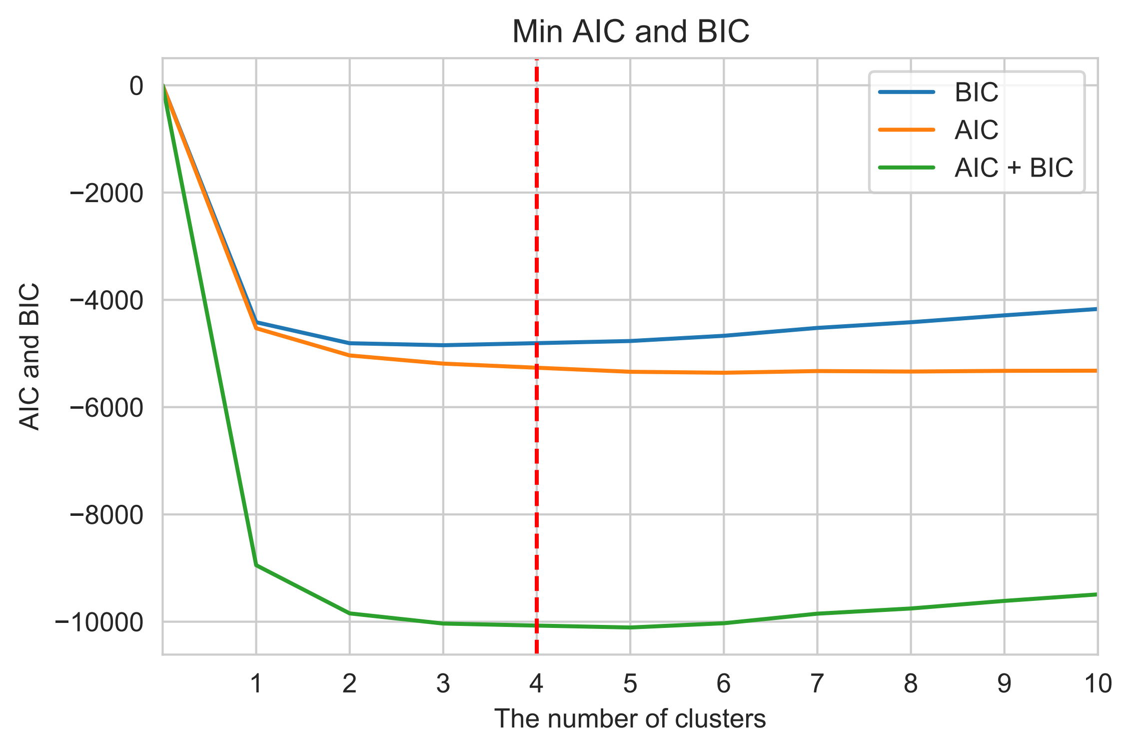
Min AIC and BIC
BIC
AIC
AIC + BIC
0
−2000
−4000
−6000
−8000
−10000
AIC and BIC
1
2
3
4
5
6
7
8
9
10
The number of clusters

Figure 12.

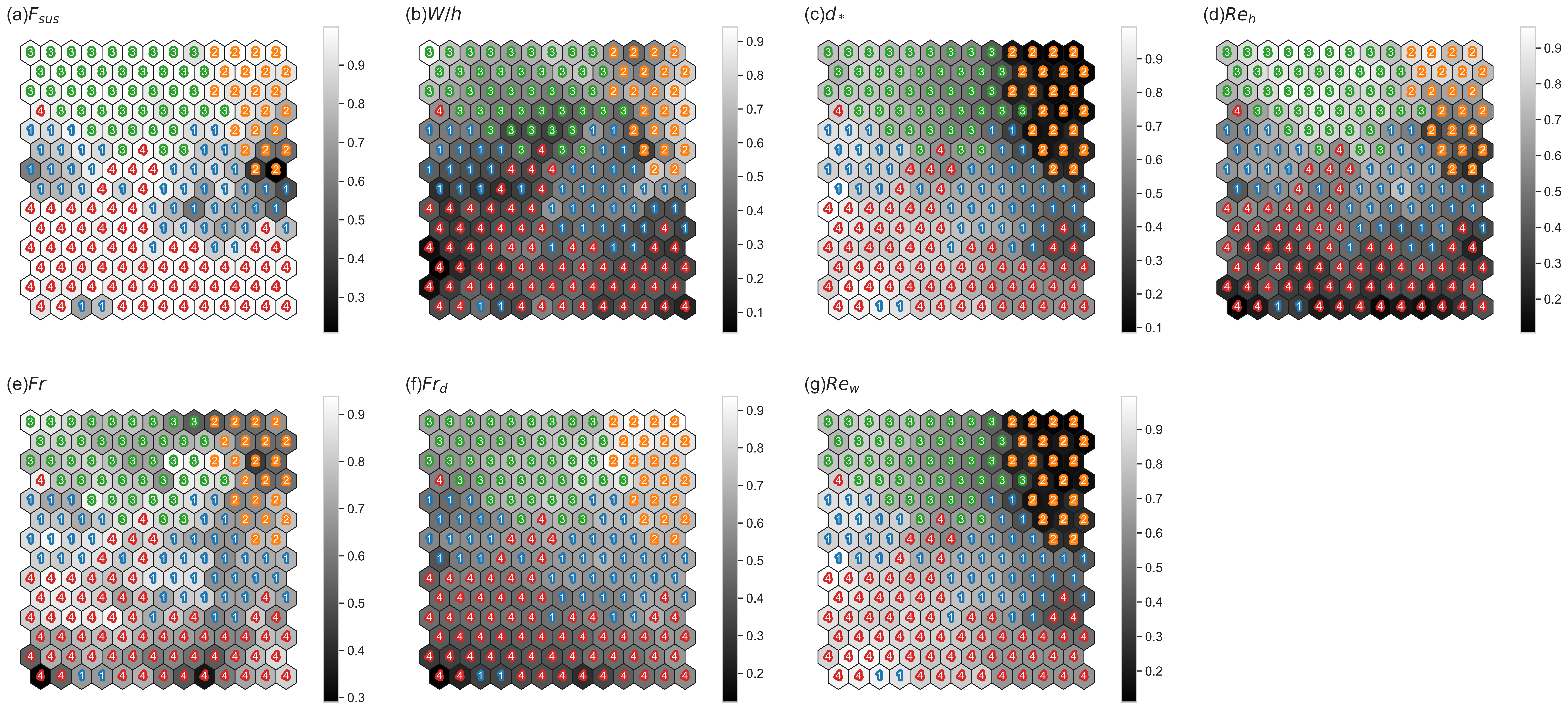

(a)F_{sus}
(b)W/h
(c)d_*
(d)Re_h
(e)Fr
(f)Fr_d
(g)Re_w

Figure 13.

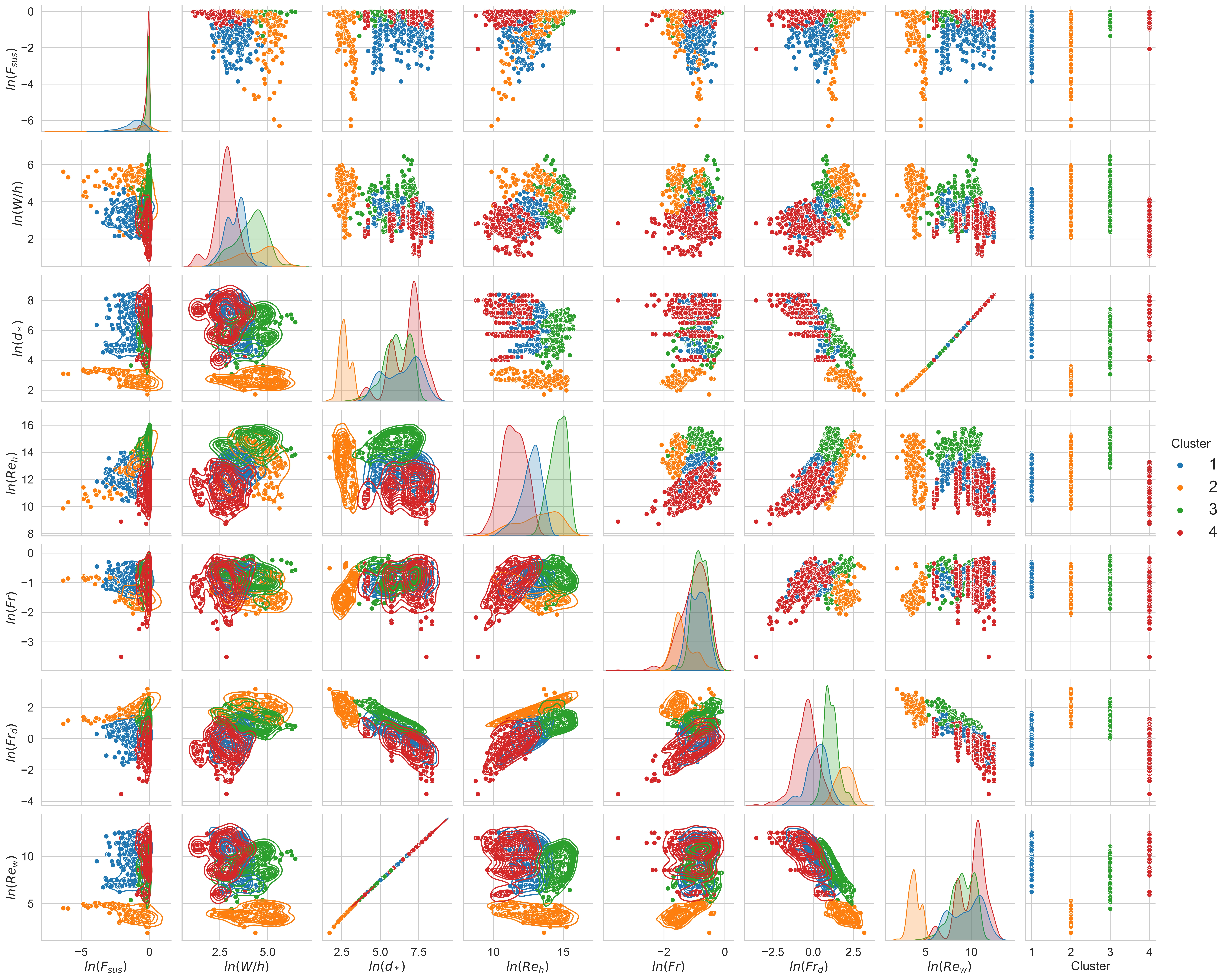

$ln(F_{sus})$
$ln(W/h)$
$ln(d_*)$
$ln(Re_h)$
$ln(Fr)$
$ln(Fr_d)$
$ln(Re_w)$
Cluster
Cluster
1
2
3
4

Figure 14.

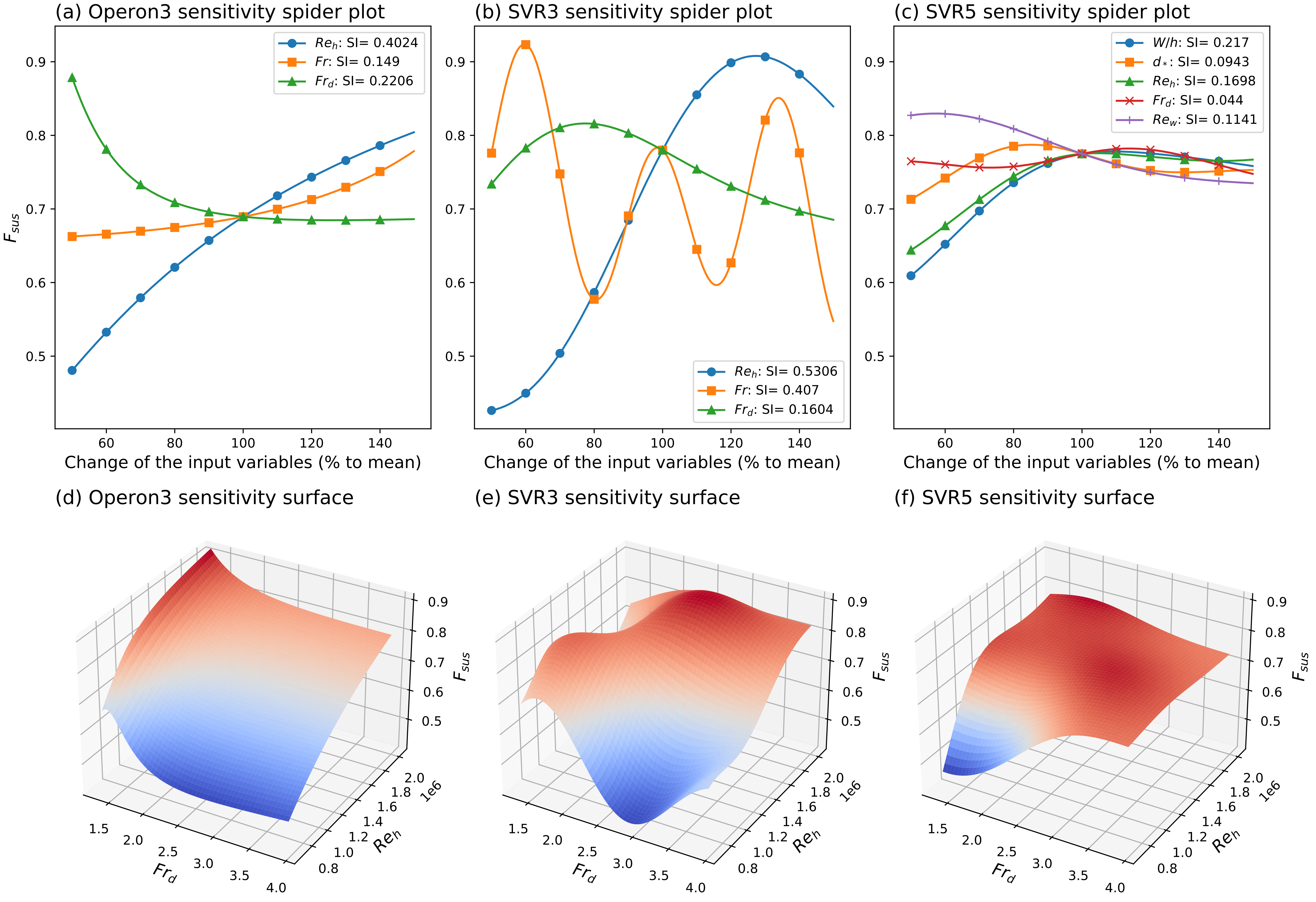
(a) Operon3 sensitivity spider plot
Re_h: SI= 0.4024
Fr: SI= 0.149
Fr_d: SI= 0.2206
F_{sus}
Change of the input variables (% to mean)
(b) SVR3 sensitivity spider plot
Re_h: SI= 0.5306
Fr: SI= 0.407
Fr_d: SI= 0.1604
Change of the input variables (% to mean)
(c) SVR5 sensitivity spider plot
W/h: SI= 0.217
d_*: SI= 0.0943
Re_h: SI= 0.1698
Fr_d: SI= 0.044
Re_w: SI= 0.1141
Change of the input variables (% to mean)
(d) Operon3 sensitivity surface
(e) SVR3 sensitivity surface
(f) SVR5 sensitivity surface
Fr_d
Re_h
1e6
F_{sus}

Figure 15.

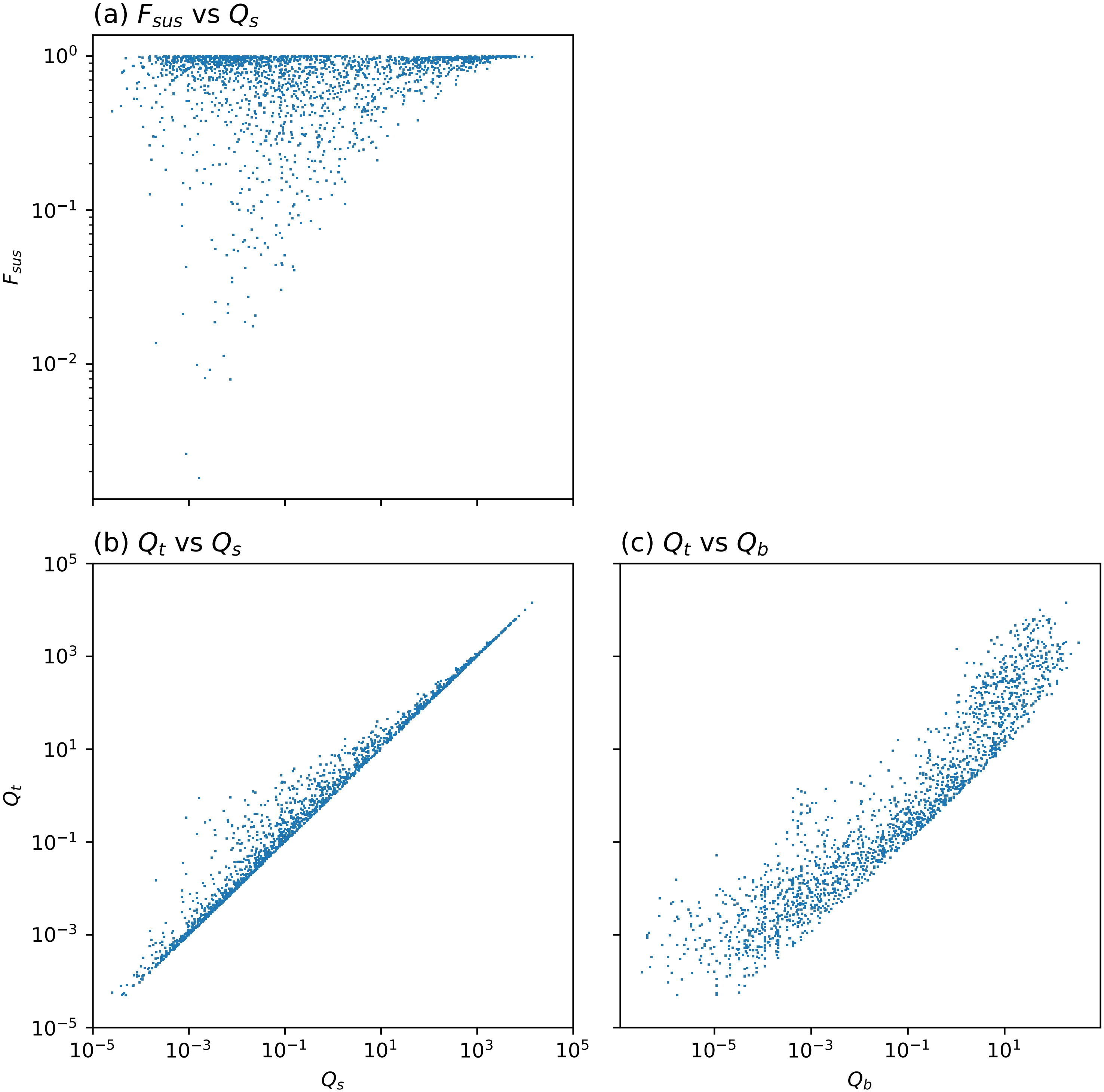
(a) F_{sus} vs Q_s
F_{sus}
10^0
10^{-1}
10^{-2}
(b) Q_t vs Q_s
Q_t
Q_s
10^{-5}
10^{-3}
10^{-1}
10^1
10^3
10^5
(c) Q_t vs Q_b
Q_b